NANO · MICRO small
www.small-journal.com

Highly Occupied Surface States at Deuterium-Grown Boron-Doped Diamond Interfaces for Efficient Photoelectrochemistry

Michał Sobaszek, Maria Brzhezinskaya,* Adrian Olejnik, Vincent Mortet, Mahebub Alam, Mirosław Sawczak, Mateusz Ficek, Maria Gazda, Zdeněk Weiss, and Robert Bogdanowicz*

Polycrystalline boron-doped diamond is a promising material for high-power aqueous electrochemical applications in bioanalytics, catalysis, and energy storage. The chemical vapor deposition (CVD) process of diamond formation and doping is totally diversified by using high kinetic energies of deuterium substituting habitually applied hydrogen. The high concentration of deuterium in plasma induces atomic arrangements and steric hindrance during synthesis reactions, which in consequence leads to a preferential (111) texture and more effective boron incorporation into the lattice, reaching a one order of magnitude higher density of charge carriers. This provides the surface reconstruction impacting surficial populations of C—C dimers, C—H, C=O groups, and —COOH termination along with enhanced kinetics of their abstraction, as revealed by high-resolution core-level spectroscopies. A series of local densities of states were computed, showing a rich set of highly occupied and localized surface states for samples deposited in deuterium, negating the connotations of band bending. The introduction of enhanced incorporation of boron into (111) facet of diamond leads to the manifestation of surface electronic states below the Fermi level and above the bulk valence band edge. This unique electronic band structure affects the charge transfer kinetics, electron affinity, and diffusion field geometry critical for efficient electrolysis, electrocatalysis, and photoelectrochemistry.

1. Introduction

To date, boron-doped diamond (BDD) interfaces are receiving continual scientific attention due to their outstanding properties, such as mechanical stability, and their electrical and optical properties.[1–3] Diamond films are grown mainly from a gas phase consisting of hydrogen, carbon, and a dopant source by microwave plasma-assisted chemical vapor deposition (MWPACVD) or hot filament chemical vapor (HFCVD) deposition. The gas composition during the growth has a significant influence on the surface morphology and the physicochemical properties of the BDD films.[4,5] The boron atoms replace some of the carbon atoms in the tetrahedral structure of the diamond, resulting in electrical conductivity from a semiconductive to the metallic state being observed as the boron-doping level (B) increases from 10^{16} to 10^{21} cm^{-3}.[6,7] This is due to electronic states being formed within the diamond band gap (5.5 eV), where the boron

M. Sobaszek, A. Olejnik, M. Ficek, R. Bogdanowicz
Gdańsk University of Technology
Faculty of Electronics
Telecommunications and Informatics
Department of Metrology and Optoelectronics
11/12 Narutowicza Str., Gdansk 80–233, Poland
E-mail: micsobas@pg.edu.pl

M. Brzhezinskaya
Helmholtz-Zentrum Berlin für Materialien und Energie
Hahn-Meitner-Platz 1, 14109 Berlin, Germany
E-mail: maria.brzhezinskaya@helmholtz-berlin.de

The ORCID identification number(s) for the author(s) of this article can be found under https://doi.org/10.1002/smll.202208265.

DOI: 10.1002/smll.202208265

V. Mortet, M. Alam
Czech Technical University in Prague
Faculty of Electrical Engineering
Technická 1902/2, Prague 6 166 27, Czech Republic

M. Sawczak
The Szewalski Institute of Fluid-Flow Machinery
Polish Academy of Sciences
Fiszera 14, Gdansk 80–231, Poland

M. Gazda
Department of Solid State Physics
Faculty of Applied Physics and Mathematics
Gdańsk University of Technology
Narutowicza 11/12, Gdańsk 80–233, Poland

Z. Weiss
CSc
FZU – Institute of Physics of the Czech Academy of Sciences
Na Slovance 2, Praha 8 182 21, Czech Republic

atoms act as acceptors at around 0.37 eV above the valence band, thus forming a *p*-type semiconductor.[8] It should be noted that only a small fraction (≈0.2%) of boron acceptors are ionized at room temperature due to the high bonding energy.

It is worth noting that in electrochemical applications such as electrolysis, electrocatalysis, and photoelectrocatalysis, the influence of the boron concentration, surface termination, and different crystal facets must be acknowledged.[9–16] Moreover, polycrystalline films contain various crystal facets, which are considered to affect electrochemical behavior.[17,18] The different facets will be impacting several diamond properties, following the well-known fact that boron species are easiest to incorporate into the following series (111) → (110) → (100). This phenomenon also translates into the response of the electrochemical redox system where the response decreases in the same series (111) → (110) → (100)-face for the inner- and outer-sphere redox markers $[Fe(CN)_6]^{3-/4-}$ and $[Ru(NH_3)_6]^{2+/3+}$, respectively.[19] Invandini et al. studied the electrochemical influence of different crystal facets of (100) and (111) homoepitaxial single-crystal BDD with similar amounts of boron, as well as polycrystalline BDD films. The authors showed that at both H- and O-terminated surfaces, the (111) plane was more reactive than the (100) plane.

Furthermore, the surface termination can play a significant role in the electrochemical response and application of BDD electrodes.[20,21] The surface functionalization can strongly influence the electron transfer kinetics of inner sphere redox processes, and the polarity of the surface bond results in electrostatic interactions which can raise or lower the energy levels of the valence E_{VB} and conduction bands E_{CB}.[22] The work done by Latto et al. shows that for highly boron-doped an oxygen-terminated diamond, the direct charge transfer via the valence band can be discounted and the charge transfer process must again be mediated by surface states.[12] Equally important is that the redox chemistry at oxygen-terminated high-doped and low-doped BDD indicates that the change in doping level leads to an increase in the density of surface states that participate in the charge transfer process. Hence, for oxygen-terminated diamond, it appears that it is the boron states that mediate the charge transfer between the bulk semiconductor and the redox couple.[12] The oxidized surface affects the width of the electrochemical working window and the OH^- surface species can enhance electrocatalysis.[23]

In fact, when the surface is terminated with hydrogen, the conduction-band edge lies ≈0.8–1.3 eV above the vacuum level, which is termed negative electron affinity (NEA). In contrast, oxidized diamond surfaces have positive electron affinity (PEA).[24] This phenomenon is important and unique for the role of diamond and its consequent ability to serve as a direct source of solvated electrons in water.[25,26] Solvated electrons can be readily created from BDD substrates and from thin-film diamond when these substrates are illuminated with ultraviolet light shorter than ≈225 nm, and a mixed nanodiamonds surface chemistry composed of a hydrogenated surface should be considered for improving the electron emission properties.[26]

Although many experimental and theoretical reports regarding the influence of the boron concentration, surface termination, and different crystal facets on the electrochemical properties of BDD have been published, only a limited number of studies have been performed on the effect of diamond growth and doping in a deuterium-rich plasma. The substitution of hydrogen for deuterium will influence several levels of the diamond film's properties, starting from the surface morphology, chemical composition, and electrical and electrochemical properties. It was found that the exchange of H atoms by D atoms in CH_4 and H_2 gases reduces the diamond growth rate by a factor of 2.3 and improves the film quality.[27,28] Likewise, using deuterium-rich plasma as a post-growth treatment was applied on selected homo-epitaxially grown (100) boron-doped diamond layers, resulting in conversion from highly *p*-type to *n*-type conductivity with electron concentrations of several 10^{16} cm^{-3}.[29,30] It should be emphasised that the anharmonicity of the C-H/D vibrational potential energy function and the lower zero-point energies of a C-D bond make the average C-D bond length ≈0.005 Å shorter than an equivalent C-H bond, resulting in a lower activation energy for diamond deposited in a deuterium-rich plasma.[31] This translates to a more effective boron incorporation into the diamond lattice, reaching a charge carrier density one order of magnitude higher for a sample deposited in deuterium-rich plasma.[32]

Diamond has unique electronic and chemical properties that make it an attractive material for use in catalysis, photocatalysis, and electroanalysis. One of the key advantages of doped diamond is its high electrical conductivity induced by boron, which makes it an excellent electrode material for electroanalysis. Diamond is also a very stable material that can withstand harsh chemical environments and high temperatures, making it suitable for use in a wide range of electrochemical applications. Additionally, diamond is chemically inert, which means it is resistant to corrosion and degradation, even under harsh chemical conditions. This makes it particularly useful for long-term photocatalytic reactions where other materials may degrade or corrode over time at a relatively low price for polycrystalline films.[33]

Moreover, many of the materials used in catalysis are subject to limitations due to their scarcity or geopolitical risk, which can make their supply unreliable or lead to price volatility. These materials are often referred to as critical raw materials (CRMs), and their limitations can pose a significant challenge to the development of sustainable catalytic processes. Diamond is one such alternative material that has shown promise in catalysis due to its unique electronic and chemical properties providing more active sites for catalytic reactions, and its electronic properties that can be tuned by doping or surface chemistry.[34]

The purpose of this extensive work is to investigate the influence of deuterium-rich plasma on the surface states in boron-doped diamond, affecting a number of electrode properties, such as charge transfer resistance, redox pair response, electron affinity, and electrochemical performance. This detailed analysis and comparison of BDD@H (hydrogen-rich plasma) and BDD@D (deuterium rich-plasma) were carried out by high-resolution X-ray photoelectron spectroscopy (XPS) and high-resolution Near-edge X-ray absorption fine structure (NEXAFS) spectroscopy supported by X-ray powder diffraction (XRD), Raman spectroscopy, and glow discharge optical emission spectroscopy (GDOES). Diffusion field geometry studies were also performed using inner- and outer-sphere redox pairs, i.e., $[Fe(CN)_6]^{4-/3-}$ and $[Ru(NH_3)_6]^{2+/3+}$, respectively. Furthermore,

density functional theory (DFT) simulations were conducted to explain the origin of the XPS and NEXAFS spectroscopy findings, where a series of new electronic states with shifted energies were identified for BDD@D. The electronic band structure of this highly faceted sample suggests that the quantities revealed by the XPS study so far did not coincide with the standard band bending, but yet another electronic phenomenon. Thus, a series of local density of states (LDOS) were calculated for both studied surfaces utilizing (100) and (111) crystallographic orientations to evaluate the BDD@H and BDD@D samples, respectively. Different arrangements of surficial terminations, i.e., C—C dimers, C—H, and COOH groups, were extensively explored, involving the kinetics of their abstraction critical to stable and efficient photoelectrochemical processes.

2. Results and Discussion

2.1. Scanning Electron Microscopy

The results of the SEM analysis are shown in **Figure 1**a–c. The direct comparison reveals differences in surface morphology between the diamond samples deposited in the hydrogen and deuterium environments. The average grain size is higher than for BDD@H than for BDD@D by ≈100 nm. The mean size of the grains is 440 and 550 nm for BDD@H and BDD@D, respectively. This can be explained by the higher process temperature caused by ionizing deuterium gas. The similar effect was observed by Mizouchi et al. showing larger heat is transferred to the sample in the D_2 synthesis compared with that in the H_2.[28] Moreover, boron doping influences on the morphology and structural imperfections of diamond films.[35] The heavy boron doping >5000 ppm generally results in increased unwanted nucleation on the substrate and an obvious decrease in the purity of the diamonds.[36] This is connected with the fact that as the boron concentration increases, the average grain size of the film decreases.[9] In contrast, this effect is not observable for the BDD@D films, where SEM analysis revealed that the grains are sharp and have an altered crystallographic orientation, which we further confirmed with XRD studies.

2.2. X-Ray Diffraction Analysis

Figure 1d presents the results of the XRD analysis for the BDD films deposited in the D_2/CH_4 and H_2/CH_4 gas mixtures.

Based on the position of the reflections, the unit cell parameters for both types of the films were determined. They are 3.568(1) Å and 3.570(1) Å for the BDD@H and BDD@D films, respectively. Both values are in agreement with the results obtained with a similar [B]/[C] ratio in the gas phase; a higher lattice parameter signifies a higher boron concentration.[37] It can be seen that reflections corresponding to the (111), (220), and (311) diamond lattice planes for the BDD@H and BDD@D films differ both in the relative intensities and widths. The widths of the reflections of BDD@D are significantly narrower than these corresponding to BDD@H (SI, Table S1, Supporting Information), which means that the crystallites in the BDD@D film

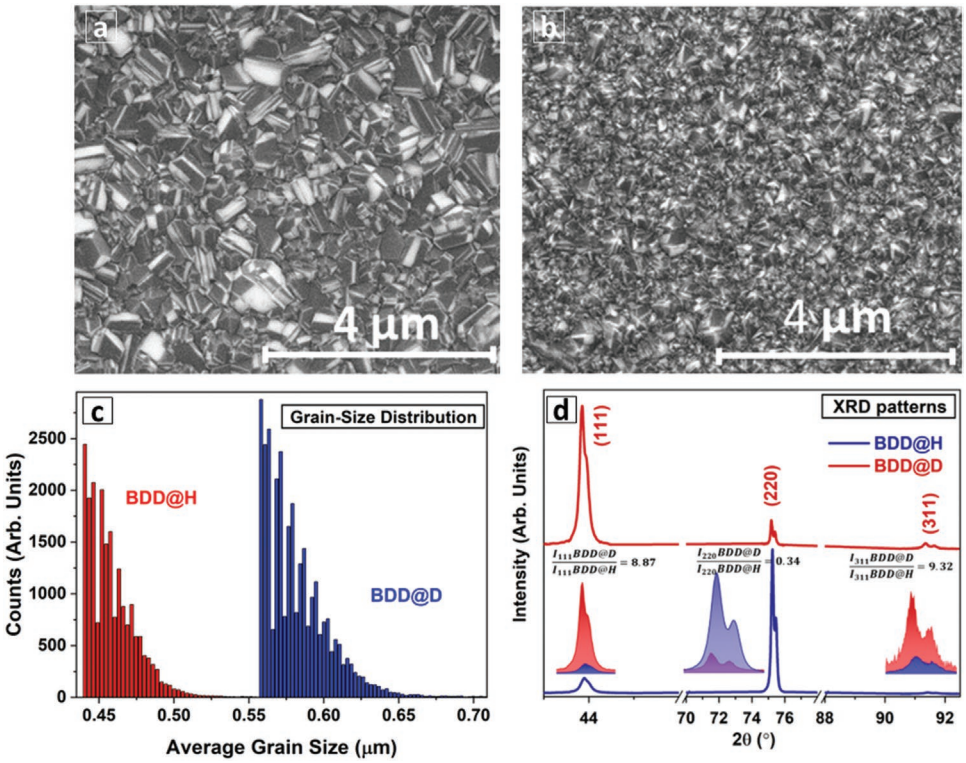

Figure 1. SEM images of a) BDD@D and b) BDD@H; c) grain size distribution among two samples; d) XRD patterns of the diamond films deposited in the D_2/CH_4 and H_2/CH_4 gas mixtures. Reflections at 2θ around 44°, 75°, and 91° correspond to the (111), (220), and (311) diamond lattice planes, respectively. Doubling of the reflections is related to the presence of Kα1 and Kα2 wavelengths in the X-ray radiation.

are larger and less strained than those in BDD@H. In both cases, the crystallites growing in the [110] directions are the largest, indicating that the orientation of the (220) planes related to the substrate surface does not influence the crystallite growth in this direction. The microstrain in the films is relatively low, with slightly decreased values for the BDD@D film. The lower microstrain in the deuterated films may be related to several factors, for instance, a lower number of grain boundaries and less non-diamond phases and impurities, e.g., boron clusters in the grain boundaries. The most spectacular differences between the films grown in the D_2/CH_4 and H_2/CH_4 gas mixtures are their orientation and texture. The ratios of intensities $\frac{I_{111}}{I_{110}}$ are 4.74 and 0.098, meaning that the (111) and (110) planes are predominantly oriented parallel to the film surface in BDD@D and BDD@H, respectively.

This may also be due to discrepancies in the texture coefficients. A texture coefficient higher than unity means that the film is textured in comparison to the polycrystalline, non-oriented material. What is interesting the BDD@D film with a relatively low ($T_c(111) = 1.29$) texture coefficient is not strongly textured in comparison to the isotropic diamond powder, however it is strongly [111] textured in comparison to the strongly [110] textured BDD@H film. The texture coefficients and microstructural details derived from the XRD patterns are described in SI.

2.3. Raman Spectroscopy

Normalized Raman spectra of the BDD@D and BDD@H thin films are shown jointly with Raman spectra recorded at different excitation wavelengths in **Figure 2**a. Both spectra exhibit the characteristic bands structure of boron-doped diamond films with a high boron concentration[38]: two broad asymmetric bands (*B*1) with maximums near $\omega = 500$ cm^{-1} (*B*1) and $\omega = 1200$ cm^{-1} (*B*2) along with the narrow diamond band (*B*3) centered near $\omega = 1330$ cm^{-1}. The wide asymmetric background with a maximum in the range from $\omega = 100$ to $\omega = 1000$ cm^{-1} is attributed to electronic Raman scattering processes.[39] The band (*B*1) is specifically sensitive to the increased boron concentration.[40] It was previously assigned to a boron dimers vibration mode.[40] The band (*B*2) with a maximum near $\omega = 1200$ cm^{-1} can be attributed to vibration modes of boron atoms,[41] however some researchers demonstrated that this band originates from vibration modes of carbon atoms,[42,43] and it is now assigned to a maximum of the phonon density of state. Independently of their assignment, these three Raman peaks have been described as Fano-shaped peaks (Figure 2b) and deconvoluted by the Breit-Wigner-Fano function—Equation (1) (see Table S2, Supporting Information):

$$BWF = \frac{H\left(1+\frac{x-x_c}{qw}\right)^2}{1+\left(\frac{x-x_c}{w}\right)^2} \quad (1)$$

The two Raman spectra are similar excepted for a higher relative intensity of the (*B*1) band for the BDD@D sample, a slight shift between the diamond peak maximum equal $\Delta_\omega = 11$ cm^{-1}, and the presence of a peak centered near $\omega = 1500$ cm^{-1} for the BDD@H sample (see Figure S1, Supporting Information). The different relative intensities might be attributed to different boron concentrations in the layers and/or different

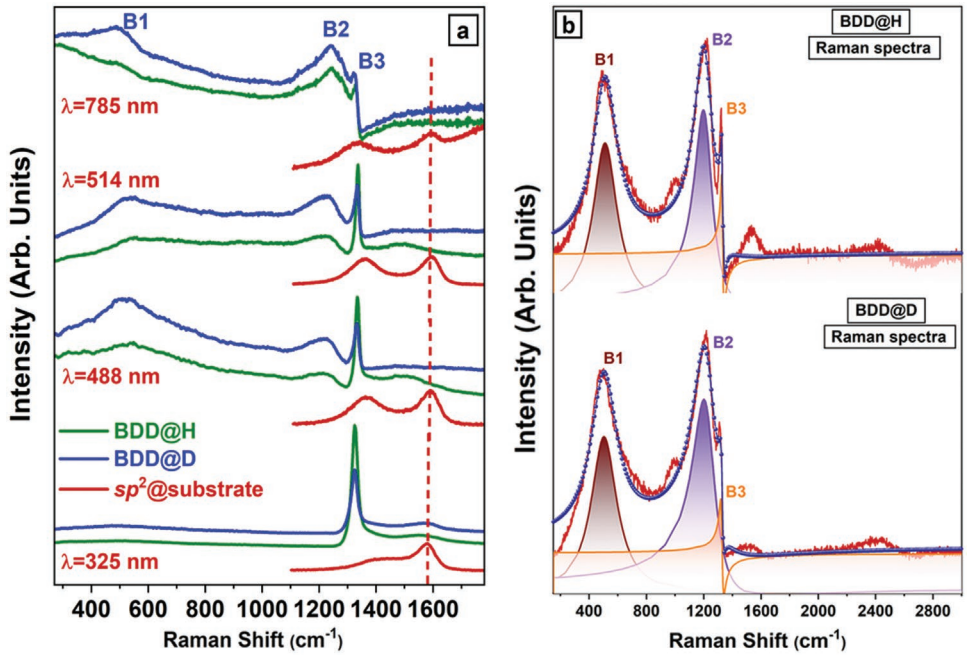

Figure 2. a) Raman spectra, recorded at different excitation wavelengths for the BDD@H and BDD@D samples. b) Normalized and modeled Raman spectra of BDD@H and BDD@D diamond films using the Breit–Wigner–Fano function, fitting different Fano-shaped peaks (B1, B2, B3) recorded at $\lambda = 514$ nm.

degrees of interaction between the electronic Raman scattering and phonon Raman scattering effect; in other words, a different asymmetric coupling coefficient, due to the different electric properties of the two types of layers. Only registered in the visible Raman spectra of the BDD@H sample, the $\omega = 1500$ cm^{-1} peak is not observed in the IR Raman spectrum of both samples and it is present in both UV Raman spectra. The peak near $\omega = 1500$ cm^{-1} was previously observed by other researchers[44–47] and assigned as the *G*-peak.[46] Yet, it is distinct from the *G*-peak by more than 50 cm^{-1} for visible laser excitations (Figure 2a), which shows the Raman spectra of the sp^2 carbon deposited on the substrate's back surface. If the origin of this peak is unclear, it might be correlated to the peak located at $\omega = 1495$ cm^{-1}, as reported by Orwa et al. when observed in ion-implanted diamond.[48] May et al.[44] and Mortet et al.[49] reported that the intensity of the *B*1 and *B*2 peaks decreases as the excitation laser's wavelength decreases, and that these bands are not observed with UV excitation. Nevertheless, the underlying origin of this phenomenon has not been definitively determined.

The boron concentration of the BDD@D samples is slightly higher ($[B] = 8.2 \times 10^{20}$ cm^{-3}) than the BDD@H sample ($[B] = 7.3 \times 10^{20}$ cm^{-3}) as determined from the average diamond peak unperturbed full wide at half maximum (FWHM) of the Raman spectra measured at different excitation wavelengths using decoupled Fano analysis of the phonon density of the state peak and the diamond.[49] Next, the visible parasitic peak around 2400 cm^{-1} is attributed to the second order of the diamond band.

The Raman spectroscopy analysis was supported by DFT simulations of pristine diamond (**Figure 3**a) and a BDD model (Figure 3b and Figure S2a, Supporting Information) using the Kubo-Greenwood formula for electrical susceptibilities and Raman tensor calculations. Broadly speaking, in the experiment, three deconvoluted peaks *B*1, *B*2, and *B*3 were observed for both the BDD@H and BDD@D samples located at $\omega \approx 500$, $\omega \approx 1200$, and $\omega \approx 1300$ cm^{-1}, respectively. For the DFT-based spectra, there is a single well-defined peak at $\omega = 1280$ cm^{-1} for a pristine diamond corresponding to the C—C stretching vibration modes (Figure 3c) and several peaks of very low intensity compared to the basic C—C stretching. This mode presumably gives the strongest contribution to the experimental *B*3 peak.

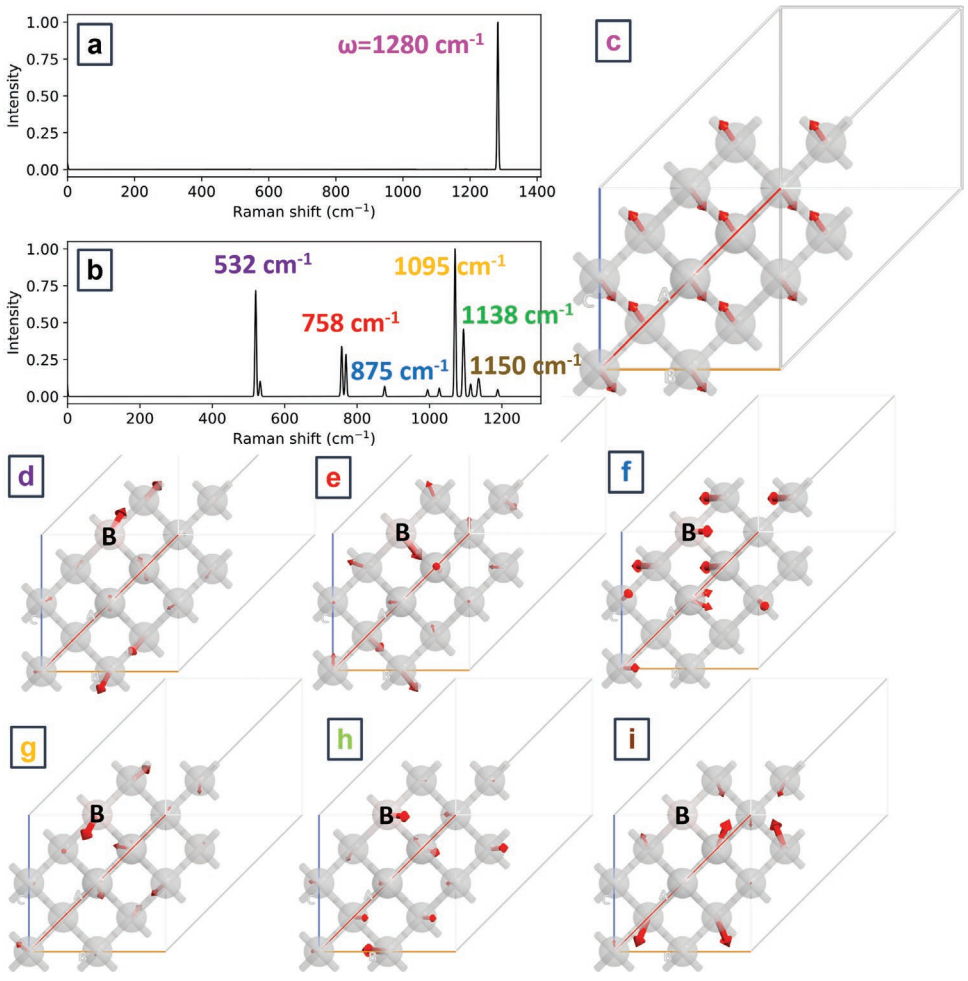

Figure 3. a,b) DFT-simulated Raman spectra of the pristine diamond and BDD model, c) vibrational mode of the pristine diamond corresponding to the $\omega = 1280$ cm^{-1} wavenumber, d–i) vibrational modes of the BDD-model corresponding to different Raman peaks. Colors correspond to the peak position marked on the spectra.

If the sample is doped by boron, a series of additional peaks appears in the spectrum at different positions. In Figure 3, they are labeled with different colors and the corresponding vibration modes are shown with respective color markings. First, the peak at $\omega = 532$ cm^{-1} corresponds mostly to C-B asymmetric stretching vibrations and some other minor modes. Although its position is slightly shifted from the experimental one, it most certainly comprises the *B*1 signal, which is in agreement with previously published works.[35] In the current model, only a single boron atom was applied in the cell (no dimers), which might have caused a slight shift in the peak position with respect to the experimental data. DFT calculations also showed a series of modes at $\omega = 758$ cm^{-1} and $\omega = 875$ cm^{-1} corresponding to different out-of-plane vibrations of boron atoms, which were not explicitly registered in the experiments. Presumably, these modes are part of the boron-sensitive *B*1 peak and, due to the relative low intensity, could not be recollected by the deconvolution. The experimental *B*2 signal consists of several modes presented in Figure 3g-i. They include both various C-B vibrations and also C-C modes of the boron neighbors, but not the boron itself, as previously suggested in Refs. [37,38]

Interestingly, the Kubo-Greenwood formula was unsuccessful in explaining the feature at $\omega = 1550$ cm^{-1} and the Fano shape of the *B*3 signal. Although C—C stretching modes of a pristine diamond provide a strong contribution to the *B*3, it must be some other source uncaptured by the conducted simulations, giving rise to the Fano shape. Particularly, in the real materials, there are some non-trivial surface defects or perhaps multiparticle states resulting from electron–phonon coupling.

2.4. X-Ray Photoelectron Spectroscopy

Figure 4 demonstrates high-resolution C1*s* (Figure 4a,c,e,g) and survey (Figure 4b,d,f,h) X-ray photoelectron spectra of BDD@H, BDD@H after annealing (BDD@H_anneal), BDD@D, and BDD@D after annealing (BDD@D_anneal), measured at $h\nu = 730$ eV. In a survey of the X-ray photoelectron spectra ($h\nu = 730$ eV) of all samples, signals from carbon and oxygen atoms can be easily seen, and a weak signal from boron atoms is also distinguishable for the BDD@H_anneal (Figure 4d) and BDD@D_anneal (Figure 4h) samples.

The C1*s* photoelectron spectrum of the BDD@H sample displays a complex structure. The spectrum of the BDD@H sample can be well described by a fitting with six components. The main component (shaded in violet), which is present in the spectrum of this sample, is located at a binding energy of 285.1 eV ($BE = 285.1$ eV) and has a symmetrical shape. This

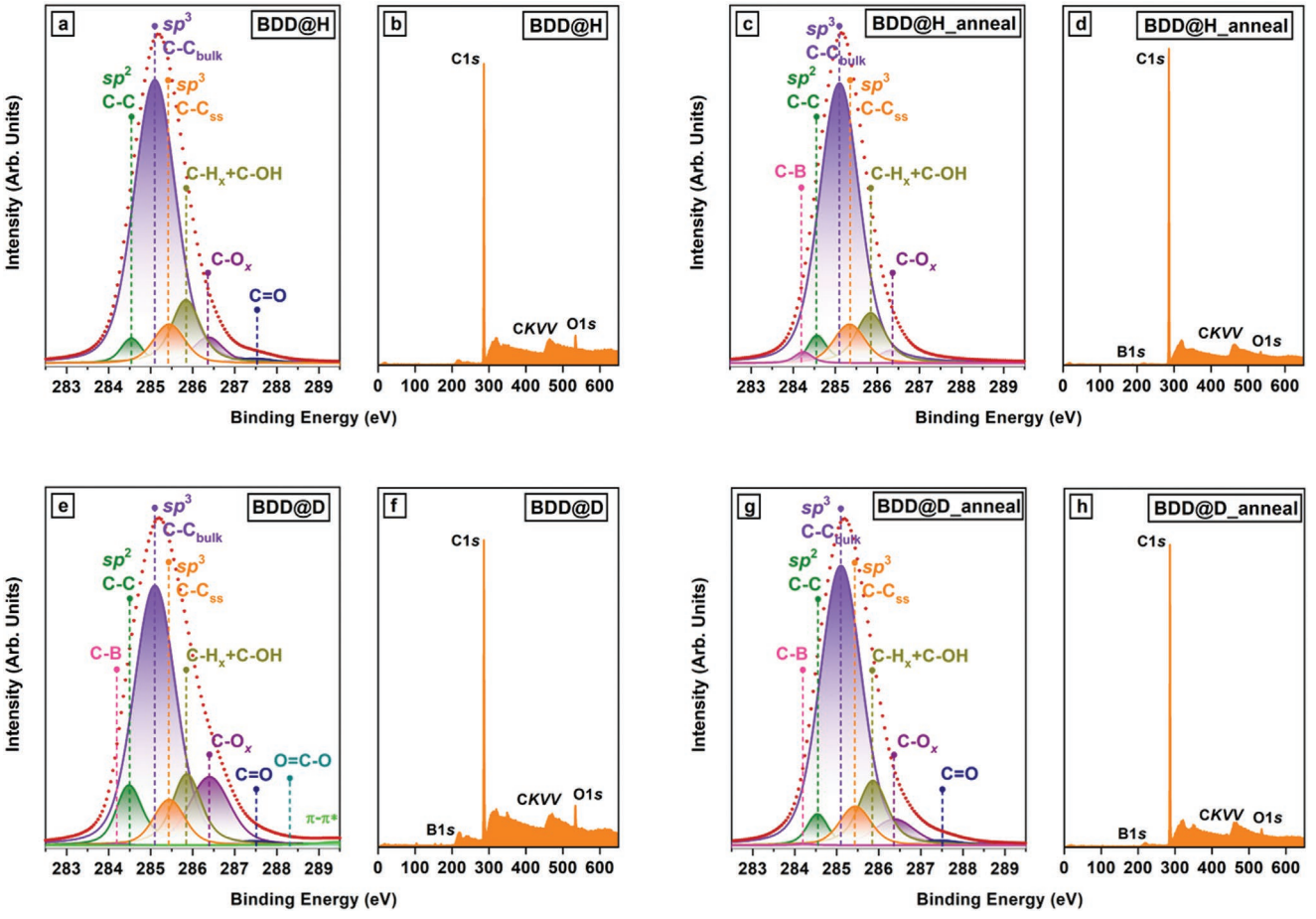

Figure 4. X-ray photoelectron spectra of the BDD@H, BDD@H_anneal, BDD@D, and BDD@D_anneal samples measured at $h\nu = 730$ eV: a,c,e,g) C1*s* spectra, and b,d,f,h) survey spectra.

Table 1. Contributions of the components in the C1*s* spectra of the BDD samples.

Sample	Peaks and their positions [eV]								
	C=C sp^2	C−C sp^3_bulk	C−C sp^3_ss	C−H_x + C−OH	C−O_x	C−B	C=O	O=C−O	π–π^*
	284.5	285.1	285.34 ÷ 285.44	285.8	286.3	284.24	287.4	288.3	289.5
BDD@H_ anneal	5.2%	72%	8.1%	10.7%	2.5%	1.5%			
BDD@H	3.4%	70.3%	7.5%	12.6%	5%	–	1.2%		
BDD@D_ anneal	4.2%	68%	7.4%	12.6%	6.3%	0.15%	1.2%		
BDD@D	10.9%	53.9%	7.3%	11.8%	14.2%	0.13%	0.9%	0.1%	0.8%

component can be uniquely identified with the C−C phase with sp^3 hybridization of the valence electron states of the carbon atoms, which are inherent in bulk diamond (C−C sp^3 bulk). The content of this phase in BDD@H is 70.3% (**Table 1**). Another component (shaded in green) is located tending toward lower binding energies from the main peak (BE = 284.54 eV) and has an asymmetric shape tending toward high binding energies. As for HOPG, it is described using the Doniach–Sunjic function and has the same asymmetry coefficient of $\alpha = 0.1$.[50] Therefore, it can be uniquely identified with the graphite C=C phase with sp^2 hybridization of the valence electron states of the carbon atoms. All other components in the C1*s* photoelectron spectrum are symmetrical. Data on the relative intensities of all major components in the deconvoluted photoelectron spectrum of the BDD@H sample, estimated by comparing the areas under the peaks, are collected in Table 1.

As can be seen from Figure 4a and Table 1, the C1*s* X-ray photoelectron spectrum of the BDD@H sample contains four more components from the side of the high binding energies. The appearance of three high-energy components in the C1*s* spectrum of BDD@H should obviously be considered as a consequence of chemical bonding between carbon, oxygen, and hydrogen atoms. This interaction leads to the formation of oxygen-containing and hydrogen-containing functional groups and is accompanied by charge transfer from carbon atoms to hydrogen and oxygen atoms due to the greater electronegativity of the latter. These three components have binding energies of 285.8 eV (shaded in yellow), 286.3 eV (shaded in purple), and 287.4 eV (shaded in navy), which correspond to chemical shifts of 1.3, 1.8, and 2.9 eV. Therefore, they can be identified with C−H_x+C−OH (hydroxyl),[50,51] C−O_x (epoxy and hydroxyl), and C=O (carbonyl) bond types.[52–54] In our opinion, most of the C−O bonds are the result of contamination both on the surface of the BDD@H sample itself, since it was prepared in the air for the XPS measurements, and on the surface of the diamond grains by the formation of chemical bonds between carbon and oxygen atoms. As can be seen from Table 1, the component with BE = 285.8 eV for the pristine BDD@H cannot be uniquely identified with either C−H_x or C−OH bonds. The total contribution of this component is 12.6%. The contributions of the C−O_x and C=O phases are insignificant and amount to 5% and 1.2%, respectively. We also assumed that we could not isolate, in the deconvoluted C1*s* photoelectron spectrum of the BDD@H sample, a component that can be identified with the presence of chemical bonding between carbon and boron atoms. It should be especially noted that the C1*s* photoelectron spectrum of the BDD@H sample contains one more component with a relative contribution of 7.5%. This component is located between the components with BE = 285.1 eV (sp^3 diamond bulk component) and BE = 285.8 eV (C−H_x+C−OH). This component (shaded in orange) is located on the side of high binding energies from the component characterizing the contribution of the sp^3 diamond bulk phase and is separated from it by 0.24 eV (BE = 285.34 eV). In one of our previous works,[55] we showed that excitation photons with an energy of 730 eV excite C1*s* photoelectrons from a depth of ≈0.85 nm. For (100)-diamond, the thickness of one monolayer is 0.089 nm.[56] Thus, the probing depth in our case is 9–10 monolayers. Naturally, the presence of various C−Ox groups indicates the presence of contaminations and impurities on the surface of diamond particles. However, in our opinion, the thickness of such contaminations and impurities cannot be more than 1–2 monolayers. Therefore, we labeled this component as sp^3 diamond surface states.

In previously published works, it is typically assumed that the component with BE = 285.4 eV can be identified with a downward band bending region at the BDD surface.[56] It is worth emphasizing that such states were previously observed only by Kono et al.[57] and Alba et al.[56]

To unambiguously answer the question about the origin of this component, the original BDD@H sample was annealed at a temperature of $T \approx 590$ K. This temperature was not chosen by chance. On the one hand, this temperature allows you to remove surface contamination from the sample surface, on the other hand, it does not lead to a change in the structure of the BDD@H sample. The C1*s* photoelectron spectrum of the BDD@H_anneal sample also has a complex structure and can also be well described by deconvolution into six components. As with the BDD@H sample, these are components with BE = 284.5 eV (sp^2 carbon), BE = 285.1 eV (sp^3 diamond bulk), BE = 285.34 eV (diamond surface states), BE = 285.8 eV (C−H_x+C−OH), and BE = 286.3 eV (C−O_x). At the same time, there is no component with BE = 287.4 eV (C=O) in the spectrum of the BDD@H_anneal sample.

The absence of the C=O component with a simultaneous strong decrease in the relative intensities of the C−Hx+C−OH component from 12.6% to 10.7% and the C-Ox component from 5% to 2.5%, and an increase in the intensities of BE to 285.1 eV (sp^3 diamond bulk) and 285.44 eV (diamond surface states) indicates the removal of a significant amount of contaminations on the surface of the BDD@H_anneal sample. Furthermore, the component that we initially identified with the diamond downward band bending region shifts by 0.1 eV toward lower binding energies (BE = 285.34 eV) after annealing. It is worth emphasizing that the spectrum of the BDD@H_anneal sample

also contains a component with BE = 284.24 eV. Its contribution is insignificant and amounts to 1.5% (Table 1). This component can be identified with the formation of a chemical bond between carbon and boron atoms.[58] This phase arises (C-B) due to charge transfer from boron atoms to more electronegative carbon atoms. The decrease in the intensity of the component with BE = 285.8 eV as a result of annealing also confirms the correctness of its identification as C—H_x+C—OH. Based on the results of the investigation by Stepan Stehlik with colleagues,[59] we can assume that ≈50% of the C—O_x bonds escaped while removing CO and CO_2 as a result of annealing so the relative concentration of C—H_x bonds can be estimated as ≈8.9%.

At the moment, the reason for the existence of a diamond band downward bending region on the surface of BDD@H_anneal has not been unequivocally established. To date, shallow acceptors with very low ionization energy, which appear due to the presence of subsurface hydrogen, have been recognized as the main hypothesis for their appearance. Further theoretical studies are undoubtedly needed to clarify the nature of the appearance of these electron states. According to Alba et al., surface transfer doping in combination with the presence of shallow acceptors very near the surface of H-terminated diamond makes it possible to describe observations of conductive layers on their surface.[56] It could be possible to also estimate the value of downward band bending as 0.24 eV at the first ≈0.85 nm of H-terminated diamond. However, in the next section, we propose an alternative explanation using surface states of diamond and boron dopant with strong computational evidence coming from the analysis of the electronic structure and projected local density of states (PLDOS).

The C1*s* photoelectron spectrum of the BDD@D sample and the spectrum of the BDD@H sample have complex structures. Unlike BDD@H, the spectrum of the BDD@D sample can be well described by deconvolution into more components, namely nine components (Table 1). The main component in the spectrum of this sample (BE = 285.1 eV) can be unambiguously identified with C=C with the sp^3-phase inherent in bulk diamond, just like in the spectrum of BDD@H. However, unlike the BDD@H sample, the content of this phase in the BDD@D sample is much lower and amounts only to 53.9% (Table 1). The spectrum contains a component with BE = 284.5 eV, which was also identified with the graphite C=C sp^2 phase. At the same time, the contribution of this phase in the BDD@D sample is almost two times higher than in the BDD@H sample and amounts to 10.9 at.%. The high content of C=C sp^2 phase in the original BDD@D sample is also confirmed by the presence of a satellite with BE ≈ 289.5 eV in the π–π^* spectrum, which is absent in the spectrum of the BDD@H sample. Characteristically, the C1*s* photoelectron spectrum of the BDD@D sample shows significantly more contaminations on the surface of BDD@D compared to BDD@H. This is evidenced by a larger number of carbon atoms that have formed a chemical bond with oxygen atoms. Namely, the contribution of the C-Ox component (BE = 286.3 eV) in the spectrum of the BDD@D sample is almost three times higher than the contribution of this component to the spectrum of BDD@H. In addition, the BDD@D spectrum also contains a component with BE = 288.3 eV (shaded cyan), which can be identified with O=C—O— (carboxyl) bond types.[52] It should be noted that the contributions of sp^3 C—C bb phase (component with BE = 285.44 eV) and C—Hx+C—OH phase (component with BE = 285.8 eV) in the BDD@D sample remain almost at the same level as in the BDD@H sample, 7.3% and 11.8%, respectively. It is important to draw attention to the fact that we were able to identify the contribution of the C-B phase in the spectrum even of the original BDD@D sample (component with BE = 284.24 eV) in contrast to the BDD@H sample, but its content is much lower, namely 0.13%.

Like BDD@H, the original BDD@D sample was also annealed at T ≈ 590 K. The C1*s* photoelectron spectrum of the BDD@D_anneal sample also has a complex structure and can be well described by deconvolution into seven components. The shape of the BDD@D spectrum after annealing (BDD@D_anneal) fully confirms our assumption that the selected annealing temperature (T ≈ 590 K) allows removing most of the contamination from the surface of the BDD@D sample without restructuring its structure. Indeed, the contribution of the C—Ox phase decreased by a factor of 2.2, similar to the BDD@H sample, and the contribution of the O=C—O phase became equal to zero. At the same time, the contribution of the C=O phase remained almost unchanged. Note that the contribution of the C—Hx+C—OH phases not only did not decrease, but even slightly increased. From our point of view, this confirms our hypothesis that the component with BE = 285.8 eV can be most likely identified with the presence of C—Hx bonds in the structure of both the BDD@H and BDD@D samples. In addition, we can conclude that the relative content of carbon atoms chemically bound to hydrogen atoms in the BDD@D sample is higher than in the BDD@H sample and can be estimated at ≈12%. The relative content of carbon atoms chemically bound to hydrogen atoms in the BDD@D sample is almost 10 times lower than in the BDD@H sample, 0.15% and ≈1.5%.

In contrast to the BDD@H sample, annealing the BDD@D sample at T ≈ 590 K leads to a sharp decrease in the content of the C=C sp^2 phase, as evidenced by a decrease in the relative intensity of the component with BE = 284.5 eV and the complete disappearance of the π–π^* satellite in the spectrum sample of the BDD@D. There is also a significant increase in the contribution of the C-C sp^3 phase inherent to bulk diamond, from 53.9% to 68%. Thus, in annealed BDD@H and annealed BDD@D, the content of this phase differs insignificantly and amounts to 72% and 68%, respectively. A similar situation is observed with the contribution of the sp^3 C—C_{ss} phase in annealed BDD@H and annealed BDD@D; the content of this phase is 8.1% and 7.4%, respectively.

Thereby, a series of new electronic states was unambiguously identified for the BDD@D samples. Their energies are shifted from the original C—C positions by 0.24 eV for BDD@H and 0.34 eV for BDD@D, respectively. Those states were previously found and attributed to downward band bending, however in the following section, we propose an alternative explanation based on DFT calculations of the surface electronic structure and surface states.

2.5. Glow Discharge Optical Emission Spectroscopy

The purpose of the Glow discharge optical emission spectroscopy (GDOES) measurements was to look for prospective

residual hydrogen/deuterium in the BDD films. As noted above, there was evidence of the (C−H_x+C−OH) bonds in the photoelectron spectra, however, due to the extreme surface sensitivity of XPS, this reflects only a few topmost monolayers and may be related to surface contamination. Two BDD samples were analyzed by GDOES in a standard experimental setup,[60] one with the possible presence of residual H/D and another—a blank sample—presumably with no H/D present. The intensity of the Lyman-α hydrogen line at 121.467 nm was recorded, with an achievable spectral resolution of ≈30 pm. The isotope shift between H and D is $\Delta\lambda = \lambda/(2.1836) = 33$ pm, i.e., isotope analysis would require deconvolution of the observed line profile or to use of another, much less sensitive line, preferably in the visible region. In our measurements, a slightly worse resolution was used, so the intensities at both wavelengths corresponding to H and D were added together. Bearing this in mind, in the text below, we will refer to this simply as "hydrogen analysis" and the quantities mentioned will be understood as corresponding to the sum H+D. The observed intensity $I_{\lambda(E),M}$ of a line at the wavelength $\lambda(E)$ of element E in the matrix M analyzed depends on the concentration c_E of this element as[60]

$$I_{\lambda(E),M} = R_{\lambda(E)}\, c_{E,M} q_M + b_{\lambda(E)} \tag{2}$$

where $b_{\lambda(E)}$ is the spectral background at the wavelength $\lambda(E)$, not related to the presence of element E in the sample, and $R_{\lambda(E)}$ is the emission yield, virtually matrix-independent, expressing the strength of the emission line used. $R_{\lambda(E)}$ and $b_{\lambda(E)}$ are calibration constants established by calibration using suitable reference samples with known concentrations of element E and known sputtering rates. Concentration c_E of element E in an unknown sample is thus

$$c_{\lambda(E),M} = \frac{I_{\lambda(E),M} - b_{\lambda(E)}}{R_{\lambda(E)} q_M} \tag{3}$$

Diamond has an extremely low sputtering rate in a glow discharge, which deteriorates the sensitivity of hydrogen analysis (i.e., a small change in the measured emission intensity reflects a large difference in the concentration, see Equation (3)). Another problem lies in determining the spectral background accurately enough.[60] In the analyses of the two samples mentioned, it was found that the observed difference in the emission intensity corresponds to the difference in the hydrogen concentration of ≈25 ppm m/m H/D (or ≈300 ppm H or ≈150 ppm D in atomic units, respectively). It should be noted that this figure is only approximate as we are close to the detection limit in this type of analysis. If the "blank" sample was hydrogen-free, this means that there was not more than ≈25 ppm m/m H/D in the other sample. This is still three orders of magnitude less than the hydrogen content in H-implanted BDD layers as analyzed by Takahara et al.[61] Although the BDD deposition occurs in a hydrogen-rich atmosphere, the process involves relatively high temperatures (several hundreds of °C), and hydrogen, if present in the growing layer, may have escaped by diffusion towards the surface before the sample cooled down.

GDOES analysis was utilized to estimate the boron concentrations in the samples, resulting in 416 ppm and 250 ppm for BDD@D and BDD@H, respectively. The Raman spectroscopy estimations revealed that boron concentration of the BDD@D samples is slightly higher ([B] = 8.2×10^{20} cm^{-3}) than the BDD@H sample ([B] = 7.3×10^{20} cm^{-3}). Both methods show that boron incorporation is enhanced in case of BDD@D. The density of diamond is approximately 3.52 g cm^{-3}, and the molar mass of boron is 10.81 g mol^{-1}. Therefore, the estimated number of boron atoms in diamond at a concentration of 416 ppm is approximately 8.16×10^{19} atoms cm^{-3}, while 250 ppm of boron in diamond corresponds to a concentration of ≈4.9×10^{19} boron atoms cm^{-3}. The lower concentration of boron observed in GDOES than Raman in BDD@H could be attributed to inhomogeneous boron localization in the intra-grain/intergrain regions followed by local density variations in case of much lower grain sizes. Raman mapping could be additionally informative to minimize the effect of spatially-oriented data delivered by Raman spectroscopy.

2.6. X-Ray Absorption Spectroscopy

Figure 5 shows the high-resolution X-ray absorption spectra acquired during this investigation for BDD@H, BDD@H after annealing, BDD@D, and BDD@D after annealing. The data obtained by HR XPS and NEXAFS spectroscopy made it possible not only to confirm the information obtained by other methods but also to study in more detail the atomic and electronic structure of the synthesised samples, as well as to characterise the chemical bonds between the atoms of chemical elements that are involved in the synthesis of BDD@H and BDD@D. It should be emphasised that, in the framework of this work, such a detailed study was carried out for the first time.

First of all, we note that the C1*s* X-ray absorption spectra of the initial BDD@H and BDD@D, and BDD@H and BDD@D after annealing are in good agreement with the spectra we measured earlier for pristine diamonds, both in terms of the number of absorption bands *A*–*F** and their energy positions.[62] This coincidence of the spectra indicates, foremost, the high quality of the atomic structure of the synthesized BDD@D and BDD@H, and the absence of noticeable impurities from amorphous and other possible carbon phases in the samples, which we showed above by XPS. This is evidenced by the almost complete absence of peak *A* in the spectrum, which is a distinctive feature of the graphite spectrum (C=C sp^2 hybridization) and is associated with dipole-allowed transitions of 1*s* electrons of the carbon atom to free states of π symmetry of the conduction band, which are formed from $\pi 2p_z$ states of carbon atoms, oriented perpendicular to the plane of the carbon layer (graphene).[63] Further, it is also confirmed by the presence of a separate *E**–*F** band (photon energy range of $h\nu$ = 303–310 eV) in the C1*s* absorption spectra of BDD@H and BDD@D, which is characteristic of the C1*s* absorption spectrum of diamond with tetrahedral coordination of carbon atoms (sp^3 hybridization) and corresponds to electronic transitions into free σ-states of the conduction band. NEXAFS spectroscopy is by far the most sensitive method to changes in the local environment of excited atoms. A more detailed examination of the presented spectra reveals some differences between the spectra of pristine diamonds, BDD@H, BDD@D, and samples after annealing.

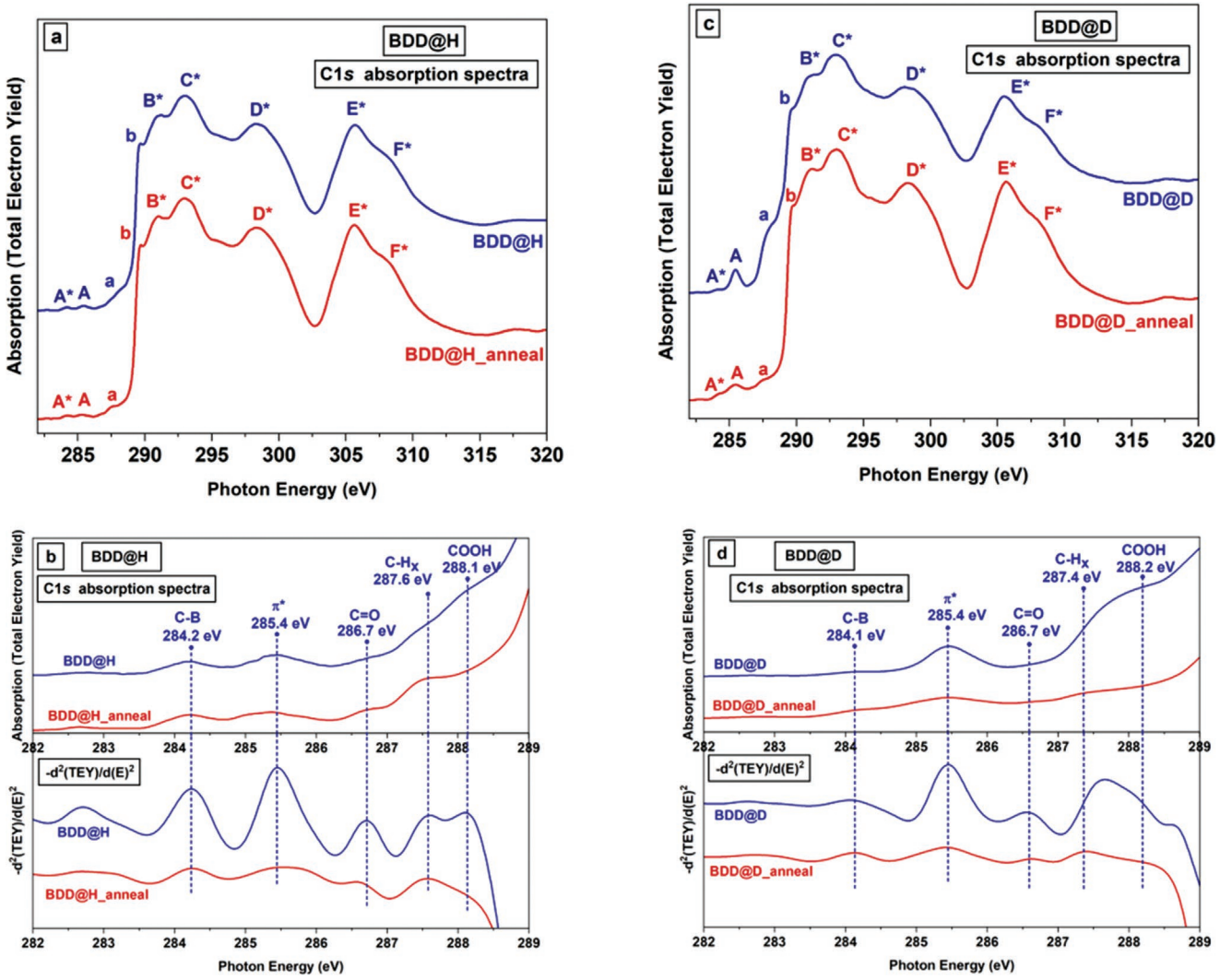

Figure 5. C1s X-ray absorption spectra of BDD@H (a,b) and BDD@D (c,d).

These differences mainly concern the details of the spectra in their low-energy part in the photon energy range of $h\nu$ = 284–289 eV. First, it should be pointed out that the intensity of the *A* band in the spectrum of BDD@D is much higher than in the spectrum of BDD@H. After annealing, the intensity of this band becomes almost the same in the spectra of both samples (BDD@D_anneal and BDD@D_anneal), which confirms our results obtained by XPS (Table 1).

Second, in the spectra of BDD@H and BDD@D, and BDD@H and BDD@D after annealing, weak *a* ($h\nu$ = 286.7 eV) and *b* ($h\nu$ = 287.6 eV) bands also appear between the *A* and *B** absorption bands. Simultaneously, a weak *A** band ($h\nu$ = 284.1÷284.2 eV) also appears in front of the *A* absorption band. On closer examination using the second derivative method, we were able, apart from that, to distinguish one more low-intensity absorption bands in all spectra with $h\nu$ = 288.2 eV (Figure 5b,d). Unlike the C1*s* X-ray photoelectron spectra,[52] the C1*s* X-ray absorption spectra make it possible to distinguish the contribution from the C—H_x phase (band with $h\nu$ = 287.4÷287.6 eV)[63] and COOH- phase (band with $h\nu$ = 288.1÷288.2 eV).[52] Hence, we unequivocally confirmed once again the presence of chemical bonding between carbon and hydrogen atoms in all samples. Moreover, in the spectrum of BDD@D, the band corresponding to the COOH phase is shifted by 0.1 eV towards higher photon energies ($h\nu$ = 288.2 eV) compared to the spectrum of BDD@H ($h\nu$ = 288.1 eV). In particular, the contribution of the COOH phase decreases after annealing of both types of samples, BDD@D and BDD@H. It should be mentioned that the (111)-faceted BDD@D surface shows a lower rate of COOH abstraction after annealing, revealing the enhanced stability also shown in the simulation data. Next, oxidized (111) diamond surfaces lead to an unconventional phenomenon, increasing both the PEA and diamond conductivity.[64] This is in agreement with the result shown by Ri et al., who showed surface conductive layers on oxidized (111) diamond with a similar characteristic to hydrogen termination.[65] Simultaneously, the band corresponding to the C-H_x phase is shifted by 0.2 eV towards lower photon energies ($h\nu$ = 287.4 eV) in the spectrum of the BDD@D compared to the spectrum of the BDD@H ($h\nu$ = 287.6 eV).

By that, it can be concluded that there is a slight difference in the strength of C—H bonds for chemical bonding between hydrogen atoms with deuterium and protium atoms; namely, the charge transfer from carbon atoms to deuterium atoms is less than from carbon atoms to protium atoms. In our opinion, the contribution of the C—H_x phase remains unchanged after annealing in the BDD@D and BDD@H samples.

The absorption band *a* ($h\nu$ = 286.7 eV) can be unambiguously interpreted as the contribution of the C=O phase formed on the surface of BDD@H and BDD@D as a result of surface contaminations.[52] This is evidenced by a significant decrease in the intensity of the *a* band after the annealing of both samples.

Of great interest is the appearance of the low-energy band *A** ($h\nu$ = 284.1÷284.2 eV) in the C1*s* X-ray absorption spectra of all studied samples. We have previously observed the appearance of this feature in the C1*s* X-ray absorption spectra of single-walled carbon nanotubes (SWNTs) intercalated with a halide of 3*d* transition metals, e.g., CuI@SWNTs.[66] We proved that the emergence of such an absorption band is a consequence of the appearance of additional electron states in CuI@SWNT, and their formation is originated from the chemical bonding between the CuI and SWNT, which occurs as a result of the hybridization of the valence electron states of the CuI and SWNT atoms. In this case, in addition to the change in occupied (bonding) valence states, new free (antibonding) states will be formed in the electron band structure of CuI@SWNT. These states will be observed in the X-ray absorption spectra of CuI@SWNT as additional bands. Therefore, we can assume that the appearance of this feature in the spectra of BDD@H, BDD@D, and samples after annealing is also a consequence of the occurrence of chemical bonding between carbon and boron atoms and of charge transfer from boron atoms to carbon atoms. Thus, we once again confirmed one of the conclusions made above by the analysis of the X-ray photoelectron spectra. Moreover, the intensity of this feature is higher in the spectra of BDD@H after annealing than in the spectra of BDD@D and BDD@D after annealing, which is consistent with the results of Table 1, that the relative contribution of the C-B phase in the sample of BDD@H_anneal is almost 10 times higher than in the BDD@D_anneal sample. Thereby, since the *A** band is observed in the spectra of BDD@H and BDD@H after annealing at $h\nu$ = 284.2 eV, and in the spectra of BDD@D and BDD@D after annealing at $h\nu$ = 284.1 eV, there is a difference in the value of charge transfer from boron atoms to carbon atoms in BDD@D and BDD@H. The B1*s* X-ray absorption spectra also confirmed the presence of boron atoms in all investigated samples (Figure S3a,b, Supporting Information).

2.7. DFT Electronic Structure Simulations

To fully understand the experimental results of the XPS and NEXAFS spectroscopy, a series of local density of states (LDOS) plots were computed for diamond and BDD in two crystallographic orientations (100)—to model the BDD@H and (111) and to model the BDD@D materials. In **Figure 6**a,b, the spatially projected electronic structure of the bulk diamond and BDD are illustrated, respectively. A set of well-defined energy levels belonging to the conduction and valence band states can be observed for both cells. For a pristine (undoped) diamond, the bandgap is equal to 4.8 eV, with the Fermi level located in the center. The value of the bandgap below the experimental ones is attributed to the well-known underestimation of the GGA functional and the fact that bandgap corrections such as DFT –½ or DFT+U were not applied in those calculations due to convergence issues and the simplicity of the surface state analyses. After boron doping with a high surface concentration of 10% (slab geometry is given in Figure S2, Supporting

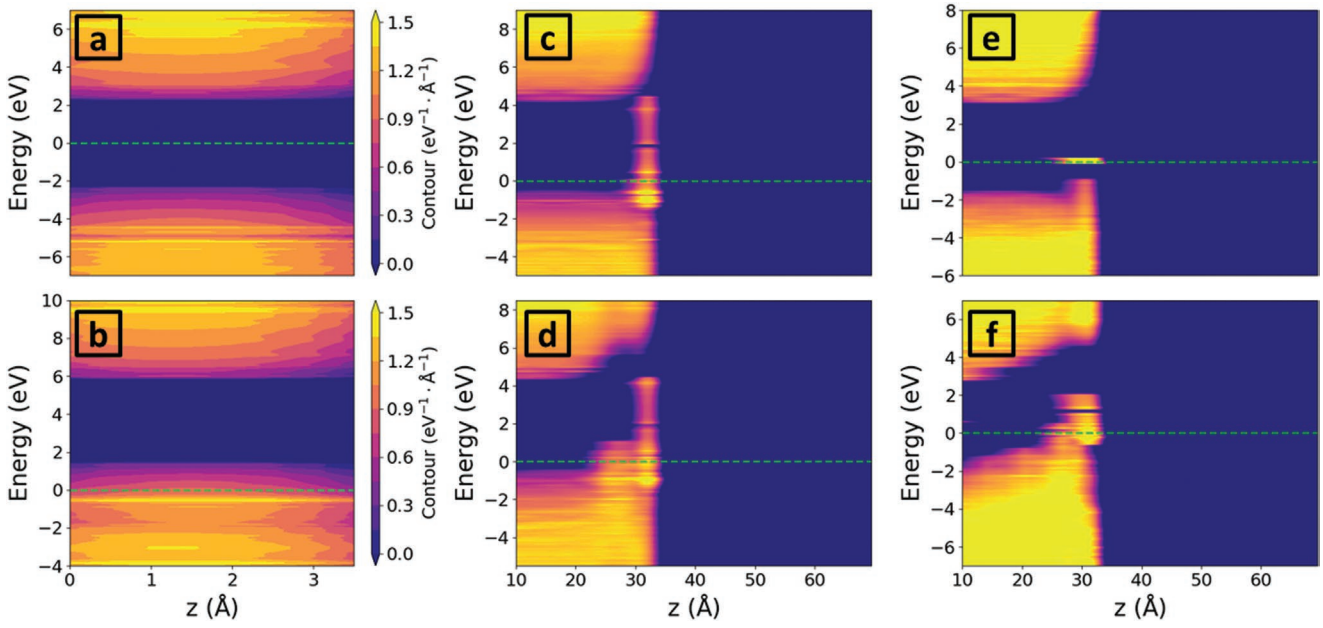

Figure 6. LDOS analyses for pristine diamond (upper panes) and BDD (lower panes) in a,b) bulk configuration, c,d) slab cut along (100) plane, e,f) slab cut along (111) plane.

Information), the bandgap decreases to 4.2 eV and the Fermi level shifts downwards into the valence band, producing quasi-metallic characteristics. This behavior was also experimentally proven,[67] with even a superconducting character below 2 K.[68]

However, in contrast to the bulk structure, when the surface is exposed, this picture changes dramatically, because a series of surface states emerges in the vicinity of the material boundary. In particular, for the (100) cut plane shown in Figure 6c, there are surface states localized in the real space between 29 and 35 Å on the *Z*-axis and quasi-uniformly distributed on the energy scale. Moreover, some of those states are distinguished by relatively high occupation (bright lines on the LDOS plot) lying below the Fermi level and corresponding to the 2*s* and 2*p* orbitals of the carbon. This fact might be a straightforward explanation of the *p*-type conduction of the (100) diamond surfaces even without the boron doping, which has been extensively reported in the literature.[56,69]

Interestingly, the energy difference (and therefore the work function difference) between the lower highly occupied surface state and the valence band edge is equal to 0.3 eV on LDOS. Considering the high occupation of the abovementioned surface state, it should be observed in the XPS spectra with ≈0.3 eV higher energy with respect to the analogous bulk state. A smaller work function should result in a higher recorded binding energy according to the principal equation of XPS:

$$E_{\text{binding}} = E_{\text{photon}} - \left(E_{\text{kinetic}} + \varnothing\right) \quad (4)$$

It is indeed in agreement with the experiment, because in Figure 4, two C—C peaks were observed with an energy difference of exactly 0.34 eV. It also stands in agreement with other experimental work,[70] where an occupied surface band entirely below the VB maximum was observed with 0.35 eV energy dispersion. Therefore, this XPS result can be interpreted as the manifestation of the bulk C—C and surface C—C states. This observation renders the standard downward band bending picture questionable. In fact, a typical signature of band bending is not observed in the presented simulations, and the conduction and valence band edges are flat. There are, however, surface states emerging as an effect of cutting the material along the (100) plane and creating the interface with vacuum. Chemically, those states can also be conceptualized as high-energy electrons resulting from dangling bonds of surface carbon atoms. This finding brings a novel viewpoint on the physics of the diamond interfaces because it strongly suggests that the quantities measured in the XPS experiments so far do not coincide with the band bending. Perhaps, other electrical phenomena are measured that are connected with the presence of surface states or crystallographic reasons.

It is to be noted that for the (111) plane, which is more abundant in the BDD@D samples, the energy difference between surface states and the VB edge is greater than for the (100) plane and equal to 0.6 eV. This was also observed in XPS experiments, although the DFT-calculated values seem to be higher, presumably originating from the application of a low-cost PBE functional. This result shows the necessity of building a new exchange-correlation function tailored specifically for studying the surface states.

With the LDOS for boron-doped diamond (Figure 6d), there is an additional set of surface states corresponding purely to the boron orbitals besides the quasi-uniform distributed surface states of carbon discussed previously. They are also localized between 22 and 32 Å on the *Z*-axis and occupy energies up to 1.5 eV over the VB edge. The Fermi level penetrates the surface states introduced by boron, similarly to the bulk case, giving rise to *p*-type conduction. Their presence can be directly correlated with the NEXAFS results showing additional electronic states of boron introduced in the BDD@D samples (absorption band *A**, 284.2 eV, Figure 5).

If the crystallographic plane of the cut is changed to (111), the distribution of the surface states is significantly altered for both pristine diamond and the BDD model (Figure 6e,f). With the undoped one, there are two types of carbon surface states—one below the Fermi level and 0.45 eV above the VB edge, and the second one in the middle of the bandgap, slightly above the Fermi level. Those two types might be viewed as shallow and deep traps, as opposed to the quasi-continuum distribution of states calculated for the (100) case. Alternatively, the (111) facet can exhibit a quasi-metallic behavior, as the Fermi level is pinned at the occupied surface band. This phenomenon was also shown experimentally using angle-resolved XPS.[71]

If, however, the boron is introduced in the (111) case, the electronic structure on the surface is significantly distorted. Initially, one could interpret the LDOS plot in Figure 6f as upward band-bending (contrary to the downward band-bending postulated in the literature). However, it is to be noted that all the energy levels remain flat and the change with respect to the (100) case is only in the position of the boron-induced surface states. The result indicates that those states are shifted upwards in the energy scale for geometric reasons induced by the change in the crystallographic plane to (111). Consequently, due to repulsion between electronic levels carbon orbitals of the conduction band are also shifted upward. It is then unambiguous that the introduction of boron into the surface layers of diamond leads to the manifestation of surface electronic states below the Fermi level and above the bulk VB edge, resulting in *p*-type conduction and standing in a good agreement with the NEXAFS spectroscopy analysis. Finally, the BDD@D sample with the (111)-dominant plane and higher boron concentration than BDD@H seems to have a richer set of surface states with higher occupation and localization.

Another step of the computational methodology was the modeling of three different surface terminations of BDD in two crystallographic orientations: (100) and (111) (**Figure 7**). The slab models used for this purpose are depicted in Figure S4 (Supporting Information). In general, for the (100) plane of BDD, hydrogenation was introduced as two hydrogen atoms attached to one of the surface carbons, and for the (111), only a single hydrogen was placed. This is due to the fulfillment of the valence rules for carbon. The case of hydroxyl termination is analogous. However, for pure C—O termination, an energetically optimal arrangement at (100) is ether C—O—C, but at (111), it is C—O with the oxygen atom perpendicular to the plane and the carbon atom extended 0.3 Å above the surface. The latter geometry presumably reflects the presence of the C—Ox peak recorded in the XPS experiments, as it does not coincide with the simple C—O bond. The fact that ether geometry is dominant on the (100) facet is known from experiments.[72] Other works suggest the same geometry should also be dominant for

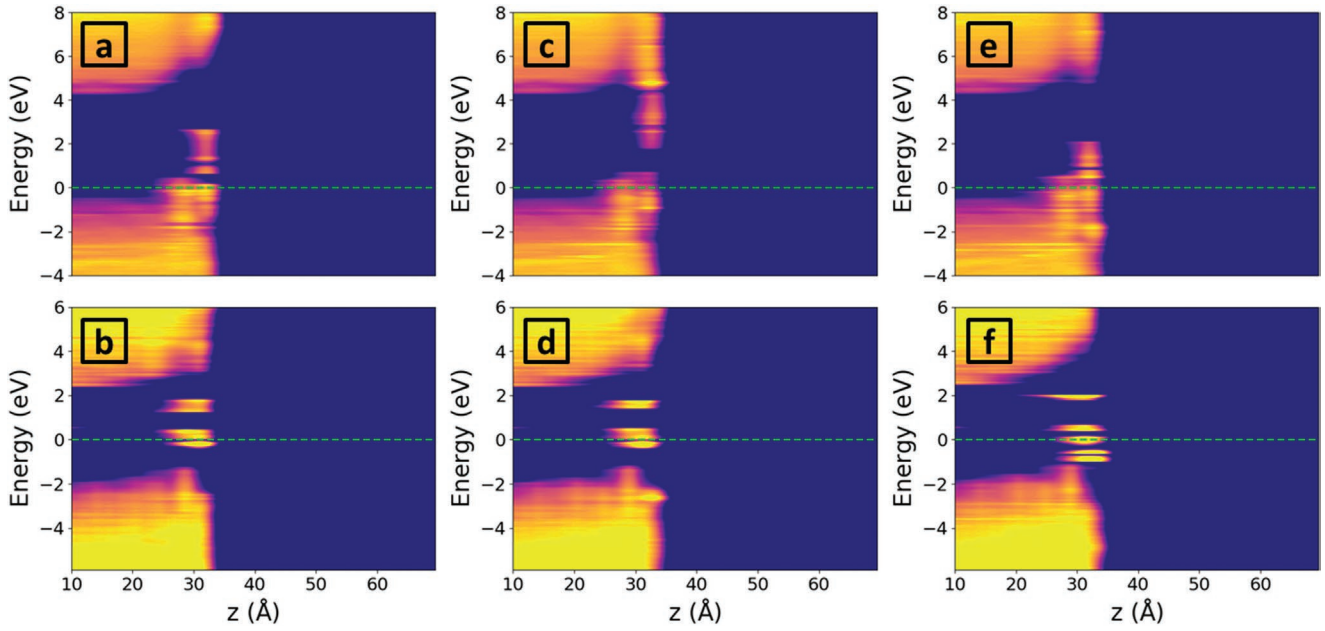

Figure 7. LDOS analyses for different terminations of BDD (100) (upper panes) and BDD (111) (lower panes) a,b) C—H-termination, c,d) C—OH termination, e,f) C—O termination. Scale bar is identical to in Figure 6.

the (111) facet of oxygenated diamond.[73] However, as the (111) facet has a stronger ability to incorporate boron at the surface, the set of results obtained from pristine diamond might not be translatable to heavily doped BDD. It is to be noted, however, that all terminations can coexist on the real surface,[74] but only C—O—C and C—O were used for the simulations for reasons of simplicity.

Gibbs free creation energies of the surface terminations were also calculated for the slabs according to the Equation (5):

$$E_{\text{creation}} = E_{\text{terminated}} - E_{\text{empty}} - E_{\text{surface atoms}} \quad (5)$$

and collected in **Table 2**. For the (100) plane, termination with the lowest free energy of creation is hydroxyl and the least favorable is ether, although the difference between hydrogen and ether is relatively small. For the (111) plane, all creation energies are lower in magnitude, indicating the weaker binding of the atoms to the surface. Analogously, the hydroxyl termination is also the most thermodynamically stable, but the least favorable one is hydrogenated. C-O termination is –1.2 eV more stable than hydrogenated, indicating the stronger affinity of oxygen to the (111) plane with respect to hydrogen. This energy difference is the anticipated cause of the fact that after annealing in a vacuum, BDD@H loses most of the oxygen, but BDD@D does not (see XPS in Figure 4). Still, hydroxyl termination is preserved in both materials and there is a change only for the C = O and C-Ox peaks. Moreover, it was also proven that the (111) facet is less prone to absorb oxygen from the air than the (100),[75] which also explains the differences in the electrochemical behavior between those two crystallographic orientations of BDD.[76]

Table 2. Gibbs free creation energies in eV of different BDD terminations calculated for (100) and (111) slabs.

Crystallographic plane	C—H	C—OH	C—O—C (100) C—O (111)
(100)	–10.77	–17.44	–10.09
(111)	–6.69	–13.35	–7.89

For the BDD (100), surface states are mostly localized at the energy range just above the VB edge and the Fermi level is pinned +0.35 eV above the VB edge. The presence and quality of the surface termination seems to have a minor influence on the position of the Fermi level. This is presumably because of the slab model construction, with a relatively high boron content serving as a reservoir of electronic levels (Figure S4, Supporting Information). On the other hand, in electrochemical experiments of pristine diamonds, it was shown that the position of the Fermi level shifts upwards after anodic treatment.[77] Therefore, the pristine diamond is expected to be prone to Fermi-level changes, and the heavily doped BDD is not.

Nevertheless, the chemistry of the termination determines the positions and relative occupations of the surface states. For the hydrogenated and oxygenated (100) BDD, there is a gap ranging from 2.8 eV to the CB edge—in contrast to the bare BDD. However, for hydroxylated BDD, this gap is located between 0.7 eV and 1.7 eV, and occupation of the electronic state just below the CB edge is higher. In other words, during mild negative (cathodic) polarisation of 0.5 V magnitude, the C—OH-terminated BDD (100) is expected to exhibit low current yield. On the other hand, the H-terminated and C—O—C-terminated BDD (100) would exhibit the same effect after strong (2 V) polarization.

BDD (111) has the Fermi level pinned down almost in the middle of the energy gap, 1.8 eV above the CB edge. For the H-terminated and C—OH-terminated ones, there are two surface bands, one crossing the Fermi level and the second one centered at 1.6 eV above the Fermi level and 0.9 eV below the CB

edge. On the other hand, for C—Ox termination, those bands are split into five bands distributed inside the bulk band gap, as shown in Figure 7f.

For all terminations, BDD is quasi-metallic because the Fermi level crosses the band formed by occupied surface states. Higher electronic occupation is observed for the BDD (111), reflecting the experimental BDD@D sample. Those characteristics should make BDD@D a prominent candidate for various electrochemical and photoelectrochemical applications, such as photoelectron emission and creating solvated electrons.[24–26] In the following section, we present an example of its potential utility in electrochemical sensing through an investigation of the diffusion field curvature.

2.8. Electrochemical Investigation

A significant feature of the BDD@D materials is their transport properties, which are relevant for electrochemical applications. In general, it is known that electrodes exhibiting high steady-state currents are prominent for application in sensing, because of the stability of the amperometric response and typically higher sensitivity towards trace amounts of analytes.[78] High steady-state currents are associated with a non-planar character of the concentration profile in the vicinity of the electrode. In other words, a closer resemblance of the concentration profile to the spherical electrode indicates a higher value of the steady-state current. The theory behind those concepts was developed two decades ago and stems from solutions to the solute transport problem to the electrode.[78–80]

Quantification of the steady-state currents can be realized in many ways. Instead of recording full steady-state voltammograms, which is a time-consuming procedure, we adopted a simple methodology allowing to capture the ratio between the steady-state current and the standard diffusion current contributions. This methodology assumes that the current measured in the voltammetry can be expressed as Equation (6):

$$j = j_{ss} + j_{diff}\sqrt{\frac{dE}{dt}} + C\frac{dE}{dt} \tag{6}$$

where j_{ss} is the steady-state current, j_{diff} is a constant proportional to the Faradaic diffusion current, which is linearly dependent on the square root of the scan rate according to the Randles–Sevcik equation, and C is a constant proportional to the scan rate, directly related to the capacitive currents. This methodology was used for studies of supercapacitors and batteries.[81–84] A higher j_{ss} to j_{diff} ratio indicates a higher contribution of the steady-state current in the total current, and a higher curvature of the concentration profile.

Figure 8a,b presents the CV curves registered for the BDD@H and BDD@D electrodes, respectively, in the presence of a ferrocyanide redox couple. A general observation is that both the oxidation and reduction peak currents increase monotonously with the scan rate and there is a high degree of symmetry between the oxidation and reduction. This fact indicates a metallic-like behavior of the BDD electrodes. This stands in agreement with DFT calculations showing that the Fermi level of BDD lies inside the occupied space (Figures 6 and 7). Therefore, surface holes/electrons are capable of both oxidation and reduction reactions for both BDD@H and BDD@D materials. The more effective incorporation of boron into the diamond lattice for BDD@D exhibited activity towards the $[Fe(CN)_6]^{3-/4-}$ redox couple, reaching peak-to-peak separation values of only 60.6 mV.[38]

The current peak plotted with respect to the scan rate was fitted according to Equation (5) with the exact values depicted in Figure 8c,d for BDD@H and BDD@D, respectively. It can be easily inferred that despite the lower magnitude of the current for BDD@D, its ratio and thus the contribution of the steady state current is greater. This result strongly suggests that in the vicinity of the BDD@D electrode, the diffusion field curvature is higher, resembling the behavior of a spherical electrode. This concept is graphically presented in Figure 8k. Another argument for this statement can be drawn from the comparative analysis of the shape of the CV curves for BDD@D and BDD@H (Figure 8f). Regardless of the scan rate, the BDD@D curves have more sigmoidal shapes, and their diffusive tails extend to larger potentials. This behavior was attributed to the higher curvature of the diffusion field also in the work of Ref. [80]

An analogous procedure was performed in the electrolyte containing a hexaammineruthenium couple instead of ferrocyanides (Figure 8g–j). The general characteristics of the CV curves are rather similar, however the enhancement of the j_{ss} to j_{diff} ratio for the BDD@D electrode is markedly larger. This phenomenon was recently observed in the work[85] and is attributed to the fact that the ruthenium couple is an Outer Sphere Electron Transfer OSET-type redox mediator and the ferrocyanides are an Inner Sphere Electron Transfer ISET-type mediator.[86] The fundamental difference lies in the fact that ISET reactants approach the electrodes more closely (to the length of several Angstroms) and their coordination environment is distorted during the electron transfer. On the other hand, OSET molecules can tunnel electrons for larger distances without geometric distortions. This makes OSET molecules more sensitive to the diffusional effects, as the main driving force of transport is diffusion rather than drift or chemical forces related with creation of surface bonds.

We hypothesize two different underlying physical causes of the shift in the diffusion field. Microscopically, it may be related to the higher energy of the boron-mediated surface states for the (111) plane (see DFT results in Figure 6) and an increased surface boron concentration (see Raman spectra in Figure 2). The high-energy surface electrons could give rise to a higher charge transfer constant (k_{CT}) locally on the crystallite edges, causing fast depletion of the depolariser in the nanometre environment of the crystallite. A similar effect of the k_{CT} dependence of the Miller plane was observed, e.g., for HOPG.[79]

Alternatively, larger crystallites of BDD@D can behave as a sparse array of microelectrodes, as opposed to the dense array of the smaller BDD@H crystallites. A sparse array corresponds to the solution of the boundary problem for the transport equation with a high steady-state current contribution, exactly as measured in the electrochemical experiments. Therefore, changes in the diffusion field geometry might be either an effect of the surface state-mediated changes in the $k_{CT,}$ or purely geometric reasons, or both.

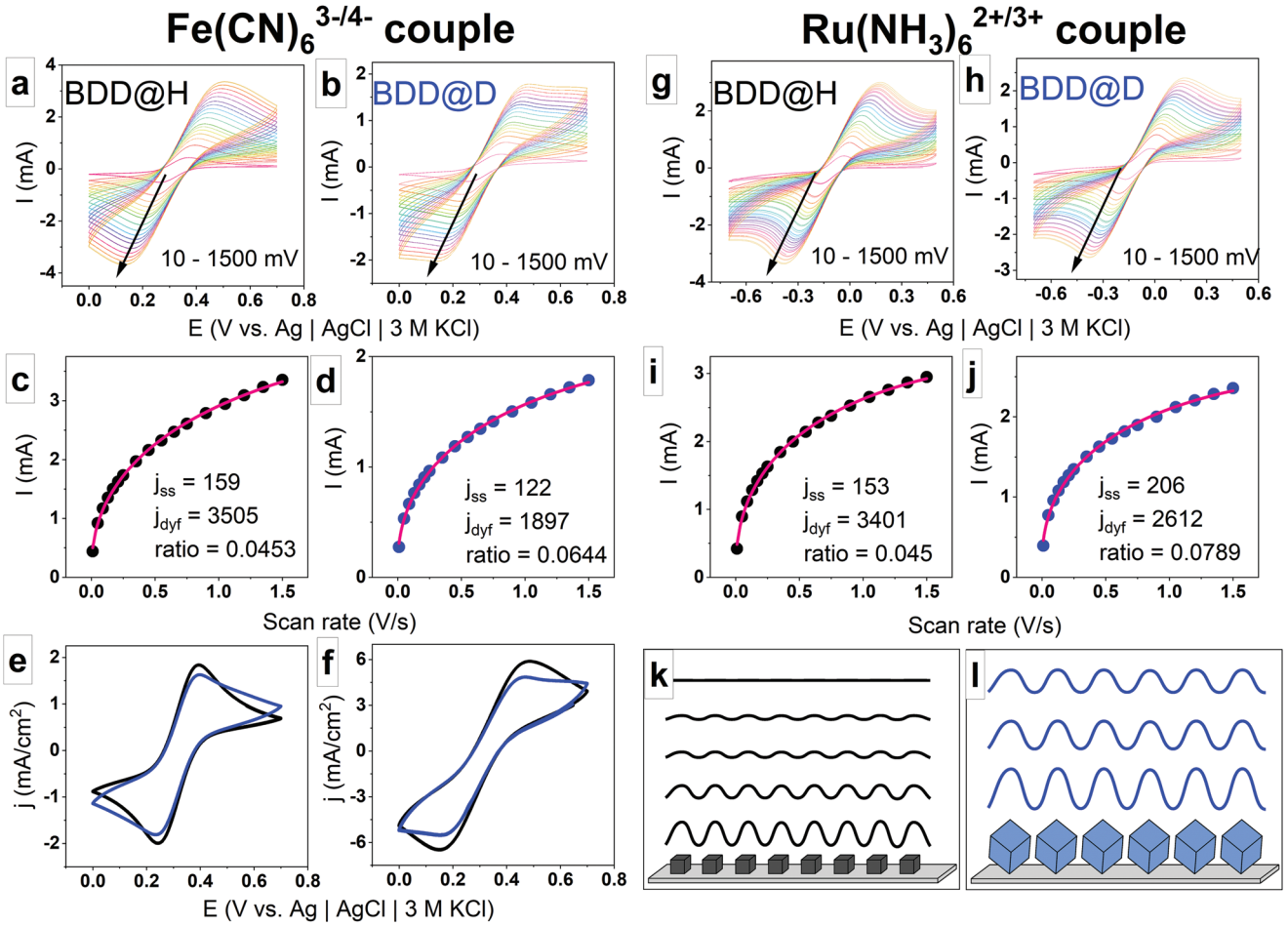

Figure 8. Electrochemical investigations of the diffusion field geometry near the BDD@H and BDD@D surfaces. a,b) Cyclic voltammetry of BDD@H and BDD@D electrodes recorded with varying scan rates in presence of 5 mM ferrocyanides; c,d) corresponding current - scan rate profiles; e,f) comparison of CV curves of BDD@H (black) and BDD@D (blue) for 100 mV/s and 1050 mV/s scan rates; g,h) cyclic voltammetry of BDD@H and BDD@D electrodes recorded with varying scan rates in presence of 2.5 mM hexaammineruthenium; i,j) corresponding current - scan rate profiles; k,l) schematic representation of the concentration gradient in the vicinity of the BDD@H and BDD@D electrodes. Red curve on the current - scan rate profiles are results of fitting according to the equation (6).

Another tool to access the diffusion field profile and steady-state current is fitting a chronoamperometric curve to the generalized Cottrell Equation (7):[85]

$$j = j_{ss} + j_C \exp\left(\frac{-t}{RC}\right) + \frac{j_F}{\sqrt{t}} \quad (7)$$

where j_{ss} is analogously, the steady-state current, which is by definition time-independent, j_C is the capacitive current related to the Heaviside step polarisation during the CA experiment, and j_F is a Faradaic Cottrell-like current decaying as a power law. The results of the fitting are given in Figure S5 (Supporting Information). In general, they are in line with the CV methodology in that the BDD-D electrodes exhibit a higher steady-state current contribution to the overall current in the presence of both redox mediators, and the difference is more prevalent in a ruthenium couple.

It is to be noted that in the following electrochemical studies, no significant differences were detected between the BDD@H and BDD@D electrodes in terms of k_{CT} calculated by either the Nicholson method or by the impedance spectroscopy. In some reports, oxygenated (111) facets tend to have slower charge transfer kinetics than (100) ones,[87] while other works report the opposite.[13] The BDD@D electrode must exhibit an interplay between kinetic enhancement by the boron doping, which is in general non-linear, and kinetic inhibition due to the accumulation of oxygen at the (111) plane induced by the presence of deuterium atoms during the CVD.[88] Analogously, the oxidation of BDD with a low amount of surface sp^2 phases shows a more irreversible process for both cathodic treatment and air-annealed surfaces.[75,89]

Because deuterium and hydrogen atoms differ only in terms of the mass of the nucleus, there are no changes in electronic energy between terminations containing hydrogen and deuterium atoms. Therefore, the influence of deuterium in the plasma during CVD on the structure and properties of the final BDD@D material is indirect. The anticipated cause of the changes induced by deuterium lies in the difference between

the C-D and C-H bond lengths.[31] This can lead to different atomic arrangements and steric hindrance during synthesis reactions and, in consequence, lead to preferential (111) geometry and simultaneously higher boron doping on the surface. The former outcome leads to slower charge transfer kinetics and C—O terminations being more stable after annealing, and enhances the electrochemical transport for geometric reasons. The latter is responsible for the quasi-metallic behavior through Fermi level pinning and increases the charge transfer kinetics. As a result, the BDD@D material represents a convenient trade-off between charge transfer kinetics and other properties acquired with boron exposure.

In addition to the electrochemical investigations focused on diffusion, a series of preliminary photoelectrochemical experiments have been performed. Figure S6 (Supporting Information) clearly shows negative photocurrents for both BDD@D and BDD@H electrodes registered during negative polarization. –800 mV polarization is required to induce the electric field inside the polycrystalline material, so that the electron–hole pairs can separate and reach contacts. As the boron-doped diamond is a p-type semiconductor, the expected photocurrents should be negative and occur mostly in the UV range in the energy region close to the band gap. Indeed, observed photocurrents are negative. However, despite the primarily large band gap of the diamond they occur also in the near UV (373 nm diode) and they are equal to –70 and –40 nA for BDD@D and BDD@H respectively. Surprisingly, only the BDD@D exhibits non-zero photocurrents even in the visible range for blue 450 nm diode (25 nA) and even for red 630 nm diode (10 nA). Those results strongly suggest a higher propensity of deuterated electrodes toward photocatalysis and due to other properties of the diamond, they are anticipated to be a reasonable choice to study electron solvation phenomena. Although photocurrent magnitudes are low, according to the best knowledge of authors they are for the first time observed in the visible range for the BDD electrode, which strongly underlines the role of surface states in tailoring the carbon-based materials.

Supplementary to the diffusion field analysis, standard electrochemical impedance spectroscopy (EIS) has been performed for both BDD@H and BDD@D electrodes (Figure S7, Supporting Information). In general, spectra for both electrodes consist of semicircles at high frequencies and straight lines at low frequencies indicating a standard EIS response of the conducting materials to the redox reactions. Although results for both electrodes are similar, the nonlinear fitting reveals a slight reduction of the charge transfer resistance R_{ct} and the magnitude of diffusion impedance A_w for the deuterated electrode. Of course, this fact highlights another advantage of the BDD@D material compared to standard BDD in electrochemical applications. The most probable explanation of this outcome is in the higher surface conductivity related to higher surface boron concentration. Double-layer capacitance is the same for both electrodes in the uncertainty margin of the fitting regardless of the deuteration. Considering the improvement is not strong (2 Ω), the main application of BDD@D is anticipated to be in photoelectrochemistry rather than electrocatalysis, especially due to its capability to produce photocurrents in different areas of the visible spectrum.

3. Conclusion

In the present work, we demonstrated that CVD process of diamond and doping is enhanced using high kinetic energies of deuterium substituting habitually utilized hydrogen. First, the deuterium in the plasma induces preferential atomic arrangements and steric hindrance during synthesis reactions, leading to a preferential (111) texture and boosted boron incorporation into the lattice of BDD@D reaching a one order of magnitude higher density of charge carriers than for BDD@H grown in hydrogen. Second, the dominating (111) facet, prone quasi-metallic behavior, as the Fermi level, is pinned at the occupied surface band and induces energetically favored surface termination by C—OH and C—Ox, as revealed using high-resolution XPS and NEXAFS spectroscopy. It was demonstrated empirically during sample annealing and proven by DFT simulation that the abstraction of C—OH and C—Ox groups is suppressed at (111)-faceted BDD@D in contrast to (110-220)-faceted BDD@H, resulting in an extremely stable charge transfer at aqueous interfaces. The D-terminated surface undergoes rapid oxidation, even at room temperature, which is confirmed by GDOES with a very small amount of D(H) terminations on the BDD@D surface.

Third, analysis of X-ray photoelectron spectra displayed the presence of well-defined electronic states previously identified with downward band bending. We proposed an alternative explanation based on the surface states of diamond and boron dopant with strong computational evidence coming from the analysis of the electronic structure and PLDOS. The bands near the BDD@D surface are rather flat, yet a set of surface states emerge inside the bandgap due to the high population of (111) facets. Moreover, the enhanced boron doping was also attributed to a rich set of highly occupied and localized surface states.

Finally, electrochemical investigations of BDD@D manifested sigmoidal shapes of a diffusion field in the vicinity of the electrode performed using inner- and outer-sphere redox pairs, presumably originating from that set of additional electronic states and beneficial for applications in electrochemical sensing. Identified highly occupied surface states strongly mediate the charge transfer behavior, redox pair performance, and electron affinity. Therefore, potential targets of BDD@D should focus on photoelectrochemistry (i.e., solvated electron generation) and bioelectroanalysis (beneficial topology of diffusion fields) rather than electrocatalysis, where the surface states and transport properties play a more important role than the charge transfer kinetics.

4. Experimental Section

Materials: The BDD@D and BDD@H were synthesized in the Microwave Plasma Assisted Chemical Vapor Deposition process. Diamond films were deposited on *p*-type (100) silicon substrates ($1 \times 1\,cm^2$). The substrates were cleaned in acetone in an ultrasonic bath for 5 min, and then washed in 2-propanol. They were then sonicated in a water nanodiamond suspension (NanoAndo, Japan). A D_2/CH_4 or H_2/CH_4 gas mixture of 1 vol.% at an overall gas flow rate of 300 sccm was used for the diamond film synthesis. The temperature of the heated stage was set to 700 °C, the process pressure to 50 Torr (6.7 kPa), and the microwave power to 1300 W. According to a previous paper the calculated growth rates 4.05 and 1.79 nm min^{-1} for the BDD@H and

BDD@D, respectively.[32] Temperature measured by pyrometer in both cases oscillates from 800 to 1000 °C. Diborane (B_2H_6) was used as a boron source. The boron doping level, expressed as the [B]/[C] ratio in the gas phase, was set to 10k ppm.

X-Ray Diffraction Analysis: The crystal structure and crystallographic orientation of the films were analyzed with a Phillips X'Pert Pro diffractometer (XRD) using Cu$K\alpha$ (1.5418 Å) radiation. The 2θ angle ranges corresponding to the (111), (220), and (311) diamond lattice crystal planes were scanned with a 0.01° step and 50 s per step. The instrumental diffraction-line broadening was determined based on the LaB6 specimen XRD profile. The broadening and shape of the reflections were evaluated in terms of the microstrain and finite crystallite size.

Scanning Electron Microscopy: The FEI Quanta FEG 250 Scanning Electron Microscope (SEM) with a 10 kV beam accelerating voltage with an SE-ETD detector (secondary electron – Everhart-Thornley detector) in high vacuum mode (pressure 10^{-4} Pa) was used to record the SEM images. The morphological studies of the mean grain size were performed on the SEM images form Figure 1a,b using the Otsu filter for the grains detection and calculated with open source software (Gwyddion 2.60, Czech Republic).

Raman Spectroscopy: Raman spectra were recorded at room temperature using a micro-Raman spectrometer (Invia, Renishaw) equipped with an edge filter with different excitation wavelengths and lasers: UV $\lambda = 325$ nm (HeCd), blue $\lambda = 488$ nm (Ar+), green $\lambda = 514$ nm (Ar+), and IR $\lambda = 785$ nm (IR diode) and 50× microscope objective. To avoid sample heating, the radiation power was set below 2 mW while the laser spot diameter on the sample surface was about 2 µm. The spectral resolution was better than 2 cm^{-1}. Each sample was analyzed at five randomly selected points and each spectrum was averaged from five measurements.

X-Ray Absorption Spectroscopy: The high-resolution C1s X-ray absorption spectra of BDD@H and BDD@D samples were measured using the facilities of the HE-SGM beamline (HE-SGM) at the BESSY II synchrotron radiation source of Helmholtz–Zentrum Berlin (HZB).[90] The measurements were carried out under ultra-high vacuum conditions: $P \approx 2\times10^{-9}$ Torr at $T = 300$ K. The NEXAFS spectra were obtained by recording the total electron yield (TEY) using PEY/TEY detector. The monochromator energy resolution near the C1s absorption edge ($h\nu \approx 285$ eV) was ≈100 meV. The size of the X-ray spot on the sample was ≈1200 × 200 µm. The photon energies in the range of the fine structure of the C1s X-ray absorption spectra were calibrated against the energy position of the first narrow peak in the C1s X-ray absorption spectrum of HOPG ($h\nu \approx 285.45$ eV).[91,92] No radiation damage of the samples was observed during the entire duration of the experiment.

X-Ray Photoelectron Spectroscopy: The X-ray photoemission spectra were acquired using a Scienta R3000 electron energy analyzer (Scienta). The C1s spectra were acquired at a photon energy ($h\nu$) of 730 eV and analyzer pass energy (*PE*) of 50 eV with an overall (monochromator and analyzer) energy resolution of ≈400 meV. The C1s, Au4*f*, and valence band spectra of the reference samples (HOPG and Au) were measured to calibrate the analyzer work function. The detection angle was close to that of normal emission. To analyze the data, the spectra were fitted by the Gaussian/Lorentzian convolution functions with simultaneous optimization of the background parameters by using the UNIFIT software.[50,93]

Electrochemical Investigations of the Diffusion Field: All electrochemical experiments were performed using a BioLogic SP-150 potentiostat–galvanostat. Measurements were conducted in electrolyte-containing 1× Tris Buffer (ChemCruz) and either 5 mM $Fe(CN)_6^{4-}/Fe(CN)_6^{3-}$ or 5 mM $Ru(NH_3)_6^{2+}/Ru(NH_3)_6^{3+}$ (Sigma–Aldrich).

BDD-H and BDD-D materials were used as working electrodes, Pt mesh as a counter electrode, and Ag | AgCl | 3 M KCl as counter electrodes. In the text, electrode potentials are expressed in terms of this reference electrode. Surface area of the BDD@H electrode was equal to 0.502 cm^2 and BDD@D to 0.326 cm^2.

For cyclic voltammetry, the scan rates were swept from 10 to 1500 mV s^{-1}. Five cycles were reported for each measurement and the last one is presented in Figures 8a,b,e-f,g-h. For chronoamperometry, Heaviside-step polarisation was applied for 300 seconds at +0.6 V for the ferrocyanides measurements and +0.3 V for the ruthenium measurements, to capture mostly oxidation currents.

All curves were fitted to the corresponding equations via nonlinear regression according to the Levenberg–Marquardt algorithm as-implemented in the Nonlinear fitting tool in the Origin software.

Electrochemical Impedance Spectroscopy: Experiments were carried out in presence of 5 mM $K_3Fe(CN)_6^{3-}$ and $K_4Fe(CN)_6^{2-}$ and 1 M KCl electrolyte in a standard three-electrode configuration with Ag | AgCl | 3 M KCl reference electrode. Before each measurement, the system was conditioned for 3 min at the formal potential of the ferrocyanides redox couple estimated from the CV measurements performed prior. Then, a frequency sweep was applied in the frequency range from 10 kHz to 100 MHz with a single sine of 10 mV amplitude as the stimulus. The EIS spectrum analyzer software was used to perform the nonlinear fitting of the results to the Randles' circuit.[94]

DFT calculations: Experimental results were supported by density functional theory (DFT) molecular modeling at the level of Generalised Gradient Approximation (GGA) using the Perdew–Burke–Ernzerhof (PBE) exchange-correlation functional and Linear Combination of Atomic Orbitals (LCAO) approach.[95] All calculations were performed using the ATK QuantumWise software. Molecular and periodic atomistic structures of MOFs were built using the implemented ATK QuantumWise builder.[96]

Raman spectra of diamond and BDD were computed using the electronic susceptibilities obtained from the DFT-based Kohn-Sham orbitals and Kubo-Greenwood formula.[97] Initial DFT calculations were performed using the norm-conserving Pseudo-Dojo pseudopotentials in high basis set,[95] a 4×4×4 *k*-point mesh and 70 Ha density mesh cut-off. Raman tensors were calculated from susceptibility derivatives in the dynamic-matrix approach using a 7×7×7 *k*-point mesh.[98] The final spectrum resulted from the addition of Raman tensors for different vibrational modes and was spherically averaged over the polarisation directions. Unit cells for this purpose contained 16 carbon atoms in a symmetry-reduced diamond *fcc* supercell and the BDD model was created through substitution of one carbon atom with boron (see Figure S1, Supporting Information, for detailed cell geometries).

Surface densities of states were computed for the pristine diamond slab and corresponding BDD model in (100) and (111) Miller cut planes. Corresponding unit cells can be found in Figure S1 (Supporting Information) and contain 71 and 119 atoms, respectively. In accordance with the experimental findings, boron atoms were substituted at the surface layers to maintain a surface concentration equal to 1/8. This value is between the one estimated from the Raman measurements (33%) and (0.42%) from GDOES. Length of the cells were equal to ≈3 nm with a 3 nm vacuum. Calculations were performed at the GGA-PBE level with Fritz-Haber Institute (FHI) norm-conserving pseudopotentials on a double zeta polarised basis.[99] Relaxation was performed using a 4×4×1 *k*-point mesh and 75 Ha density mesh cut-off, and the density of states was calculated using a 7×7×1 *k*-point mesh. Local density of states spectra were computed by projecting the total density of states of the system on the spatial coordinate as implemented in the ATK package. Zero energy is placed at the Fermi level according to the Fermi-Dirac occupation function. While the length of the diamond/BDD part of the cell equaled 3 nm, only 2 nm are presented on the LDOS for clarity, due to distortions connected with the boundary conditions used for solving the Poisson equation during the DFT procedure. Bandgap corrections such as DFT+U and DFT-½ were not applied to the surface calculations for reasons of convergence.[100] For studies of different surface terminations of BDD, analogous slab models were applied with the following set of surface atoms added. For the (100) slab, two hydrogen atoms, or one hydrogen atom, and one OH group, or one oxygen atom were placed. For the (111) slab, one hydrogen, one OH group, and one oxygen atom were placed. Those differences stem from the necessity of satisfying the valence rules for carbon atoms. All slabs were relaxed after surface modifications with 0.05 eV $Å^{-1}$ force tolerance.

Glow Discharge Optical Emission Spectroscopy: Glow discharge emission spectra were measured using a GDA750HR spectrometer (Spectruma GmbH, Germany), with a *dc* discharge in argon in a 2.5 mm-internal anode diameter Grimm-type spectral source.[60] The optical system of the instrument consisted of a $f = 0.75$ m Paschen-Runge vacuum polychromator with 34 fixed channels with photomultipliers. A constant discharge voltage/constant current of 850 V/15 mA was used in the measurements, the voltage was stabilized electronically and the current was stabilized by a feedback loop, by adjusting the flow (pressure) of the working gas. Calibration for the carbon and boron was based on certified reference materials (CRMs) largely of ferrous matrix (steels and cast irons). Emission yield of the H I, 121.467 nm line used for hydrogen analysis was established based on a sample of hydrogenated titanium with a TiH_2 layer on the surface and a sample of high-purity titanium.

Supporting Information

Supporting Information is available from the Wiley Online Library or from the author.

Acknowledgements

M.S., M.B., and M.F. thank Helmholtz-Zentrum Berlin (HZB) for the allocation of synchrotron radiation beamtime at HZB (Germany). M.S. gratefully acknowledges the financial support of these studies from the Gdansk University of Technology through the DEC-02/2021/IDUB/II.1/AMERICIUM grant under the Americium – "Excellence Initiative – Research University" program. V.M. acknowledges the funding from the 20–11140S project of the Czech Science Foundation. R.B. acknowledges the funding from the National Science Centre, Poland under the OPUS call in the Weave programme (Project number: 2021/43/I/ST7/03205).

Open access funding enabled and organized by Projekt DEAL.

Conflict of Interest

The authors declare no conflict of interest.

Data Availability Statement

The data that support the findings of this study are available from the corresponding author upon reasonable request.

Keywords

core-level spectroscopies, deuterium-based plasma, density functional theory (DFT) calculations, polycrystalline diamonds, Raman spectroscopy

Received: December 30, 2022
Revised: March 3, 2023
Published online:

[1] N. Yang, G. M. Swain, X. Jiang, *Electroanalysis* **2016**, *28*, 27.
[2] D. Liang, W. Yan-Hui, Z. Jian-Bing, *J. Inorg. Mater.* **2017**, *32*, 673.
[3] Y. V. Pleskov, M. D. Krotova, V. V. Elkin, E. A. Ekimov, *Electrochim. Acta* **2016**, *201*, 268.
[4] S. Garcia-Segura, E. Vieira dos Santos, C. A. Martínez-Huitle, *Electrochem. Commun.* **2015**, *59*, 52.
[5] N. R. Wilson, S. L. Clewes, M. E. Newton, P. R. Unwin, J. V. Macpherson, *J. Phys. Chem. B* **2006**, *110*, 5639.
[6] W. Gajewski, P. Achatz, O. A. Williams, K. Haenen, E. Bustarret, M. Stutzmann, J. A. Garrido, *Phys. Rev. B* **2009**, *79*, 045206.
[7] J.-P. Lagrange, A. Deneuville, E. Gheeraert, *Diamond Relat. Mater.* **1998**, *7*, 1390.
[8] A. Fujishima, Y. Einaga, T. N. Rao, D. A. Tryk, *Diamond Electrochemistry*, Elsevier, Cham, Switzerland **2005**.
[9] X. Z. Liao, R. J. Zhang, C. S. Lee, S. T. Lee, Y. W. Lam, *Diamond Relat. Mater.* **1997**, *6*, 521.
[10] H. Long, H. Luo, J. Luo, Y. Xie, Z. Deng, X. Zhang, Y. Wang, Q. P. Wei, Z. M. Yu, *Mater. Lett.* **2015**, *157*, 34.
[11] K. Asai, T. A. Ivandini, M. M. Falah, Y. Einaga, *Electroanalysis* **2016**, *28*, 177.
[12] M. N. Latto, G. Pastor-Moreno, D. J. Riley, *Electroanalysis* **2004**, *16*, 434.
[13] T. A. Ivandini, T. Watanabe, T. Matsui, Y. Ootani, S. Iizuka, R. Toyoshima, H. Kodama, H. Kondoh, Y. Tateyama, Y. Einaga, *J. Phys. Chem. C* **2019**, *123*, 5336.
[14] J.-M. Cho, Y.-J. Ko, H.-J. Lee, H.-J. Choi, Y.-J. Baik, J.-K. Park, J. Y. Kwak, J. Kim, J. Park, Y. Jeong, I. Kim, K.-S. Lee, W.-S. Lee, *Small* **2022**, *18*, 2105087.
[15] R. Guo, J. Wang, Z. Bi, X. Chen, X. Hu, W. Pan, *Small n/a*, 2206314.
[16] S. Handschuh-Wang, T. Wang, Y. Tang, *Small* **2021**, *17*, 2007529.
[17] S. Yu, S. Liu, X. Jiang, N. Yang, *Carbon* **2022**, *200*, 517.
[18] T. Kondo, *Curr. Opin. Electrochem.* **2022**, *32*, 100891.
[19] Y. V. Pleskov, Y. E. Evstefeeva, M. D. Krotova, V. P. Varnin, I. G. Teremetskaya, *J. Electroanal. Chem.* **2006**, *595*, 168.
[20] O. A. Williams, R. B. Jackman, *Semicond. Sci. Technol.* **2003**, *18*, S34.
[21] R. B. Jackman, H. J. Looi, L. Y. S. Pang, M. D. Whitfield, J. S. Foord, *Carbon* **1999**, *37*, 817.
[22] J. V. Macpherson, *Phys. Chem. Chem. Phys.* **2015**, *17*, 2935.
[23] J. Cai, T. Niu, P. Shi, G. Zhao, *Small* **2019**, *15*, 1900153.
[24] D. Zhu, L. Zhang, R. E. Ruther, R. J. Hamers, *Nature Mater* **2013**, *12*, 836.
[25] R. J. Hamers, J. A. Bandy, D. Zhu, L. Zhang, *Faraday Discuss.* **2014**, *172*, 397.
[26] F. Buchner, T. Kirschbaum, A. Venerosy, H. Girard, J.-C. Arnault, B. Kiendl, A. Krueger, K. Larsson, A. Bande, T. Petit, C. Merschjann, *Nanoscale* **2022**, *14*, 17188.
[27] O. Ternyak, S. Michaelson, L. Tkach, R. Akhvlediani, A. Hoffman, *phys. stat. sol. (a)* **2007**, *204*, 2839.
[28] N. Mizuochi, J. Isoya, J. Niitsuma, T. Sekiguchi, H. Watanabe, H. Kato, T. Makino, H. Okushi, S. Yamasaki, *J. Appl. Phys.* **2007**, *101*, 103501.
[29] Z. Teukam, J. Chevallier, C. Saguy, R. Kalish, D. Ballutaud, M. Barbé, F. Jomard, A. Tromson-Carli, C. Cytermann, J. E. Butler, M. Bernard, C. Baron, A. Deneuville, *Nature Mater* **2003**, *2*, 482.
[30] J. Chevallier, Z. Teukam, C. Saguy, R. Kalish, C. Cytermann, F. Jomard, M. Barbé, T. Kociniewski, J. E. Butler, C. Baron, A. Deneuville, *Phys. Status Solidi A* **2004**, *201*, 2444.
[31] J. S. Mugridge, R. G. Bergman, K. N. Raymond, *Angew. Chem.* **2010**, *122*, 3717.
[32] R. Bogdanowicz, M. Sobaszek, M. Sawczak, G. M. Grigorian, M. Ficek, P. Caban, A. Herman, A. Cenian, *Diamond Relat. Mater.* **2019**, *96*, 198.
[33] R. Bogdanowicz, *Curr Opin Solid State Mater Sci* **2022**, *26*, 100991.
[34] B. Kiendl, A. Day, S. Choudhury, F. Buchner, K. Atak, A. Chemin, C. Merschjann, E. Hadzifejzovic, T. Claridge, K. Larsson, A. Venerosy, M. Lounasvuori, N. Zabarska, B. Iliev, T. Schubert, H. Girard, J.-C. Arnault, T. Petit, J. Foord, A. Krueger, (Preprint) 10.26434/chemrxiv-2022-jm92g, v1, submitted: December **2022**.
[35] X. H. Wang, G.-H. M. Ma, W. Zhu, J. T. Glass, L. Bergman, K. F. Turner, R. J. Nemanich, *Diamond Relat. Mater.* **1992**, *1*, 828.

[36] T. Zhang, L. Wang, F. Sun, B. Shen, Z. Zhang, *Diamond Relat. Mater.* **2013**, *40*, 82.
[37] N. G. Ferreira, E. Abramof, E. J. Corat, V. J. Trava-Airoldi, *Carbon* **2003**, *41*, 1301.
[38] A. Dettlaff, M. Sobaszek, T. Klimczuk, R. Bogdanowicz, *Carbon* **2021**, *174*, 594.
[39] V. Mortet, I. Gregora, A. Taylor, N. Lambert, P. Ashcheulov, Z. Gedeonova, P. Hubik, *Carbon* **2020**, *168*, 319.
[40] M. Bernard, A. Deneuville, P. Muret, *Diamond Relat. Mater.* **2004**, *13*, 282.
[41] M. Werner, O. Dorsch, H. U. Baerwind, E. Obermeier, L. Haase, W. Seifert, A. Ringhandt, C. Johnston, S. Romani, H. Bishop, P. R. Chalker, *Appl. Phys. Lett.* **1994**, *64*, 595.
[42] N. Dubrovinskaia, L. Dubrovinsky, T. Papageorgiou, A. Bosak, M. Krisch, H. F. Braun, J. Wosnitza, *Appl. Phys. Lett.* **2008**, *92*, 132506.
[43] P. Szirmai, T. Pichler, O. A. Williams, S. Mandal, C. Bäuerle, F. Simon, *Phys. Status Solidi B* **2012**, *249*, 2656.
[44] P. W. May, W. J. Ludlow, M. Hannaway, P. J. Heard, J. A. Smith, K. N. Rosser, *Diamond Relat. Mater.* **2008**, *17*, 105.
[45] M. Bernard, C. Baron, A. Deneuville, *Diamond Relat. Mater.* **2004**, *13*, 896.
[46] S. Ghodbane, A. Deneuville, *Diamond Relat. Mater.* **2006**, *15*, 589.
[47] R. Haubner, M. Rudigier, *Phys. Procedia* **2013**, *46*, 71.
[48] J. O. Orwa, K. W. Nugent, D. N. Jamieson, S. Prawer, *Phys. Rev. B* **2000**, *62*, 5461.
[49] V. Mortet, Z. V. Živcová, A. Taylor, M. Davydová, O. Frank, P. Hubík, J. Lorincik, M. Aleshin, *Diamond Relat. Mater.* **2019**, *93*, 54.
[50] M. Brzhezinskaya, E. A. Belenkov, V. A. Greshnyakov, G. E. Yalovega, I. O. Bashkin, *J. Alloys Compd.* **2019**, *792*, 713.
[51] A. T. Dideikin, A. E. Aleksenskii, M. V. Baidakova, P. N. Brunkov, M. Brzhezinskaya, V. Y. Davydov, V. S. Levitskii, S. V. Kidalov, Y. A. Kukushkina, D. A. Kirilenko, V. V. Shnitov, A. V. Shvidchenko, B. V. Senkovskiy, M. S. Shestakov, A. Y. Vul', *Carbon* **2017**, *122*, 737.
[52] M. Brzhezinskaya, O. O. Kapitanova, O. V. Kononenko, S. Koveshnikov, V. Korepanov, D. Roshchupkin, *J. Alloys Compd.* **2020**, *849*, 156699.
[53] V. V. Shnitov, M. K. Rabchinskii, M. Brzhezinskaya, D. Y. Stolyarova, S. V. Pavlov, M. V. Baidakova, A. V. Shvidchenko, V. A. Kislenko, S. A. Kislenko, P. N. Brunkov, *Small* **2021**, *17*, 2104316.
[54] M. K. Rabchinskii, S. A. Ryzhkov, M. V. Gudkov, M. V. Baidakova, S. D. Saveliev, S. I. Pavlov, V. V. Shnitov, D. A. Kirilenko, D. Y. Stolyarova, A. M. Lebedev, R. G. Chumakov, M. Brzhezinskaya, K. A. Shiyanova, S. V. Pavlov, V. A. Kislenko, S. A. Kislenko, A. Makarova, V. P. Melnikov, P. N. Brunkov, *2D Mater.* **2020**, *7*, 045001.
[55] P. M. Valetsky, M. G. Sulman, L. M. Bronstein, E. M. Sulman, A. I. Sidorov, V. G. Matveeva, *Nanotechnol Russia* **2009**, *4*, 647.
[56] G. Alba, D. Eon, M. P. Villar, R. Alcántara, G. Chicot, J. Cañas, J. Letellier, J. Pernot, D. Araujo, *Surfaces* **2020**, *3*, 61.
[57] S. Kono, T. Kageura, Y. Hayashi, S.-G. Ri, T. Teraji, D. Takeuchi, M. Ogura, H. Kodama, A. Sawabe, M. Inaba, A. Hiraiwa, H. Kawarada, *Diamond Relat. Mater.* **2019**, *93*, 105.
[58] B. J. Matsoso, K. Ranganathan, B. K. Mutuma, T. Lerotholi, G. Jones, N. J. Coville, *New J. Chem.* **2017**, *41*, 9497.
[59] S. Stehlik, M. Varga, M. Ledinsky, V. Jirasek, A. Artemenko, H. Kozak, L. Ondic, V. Skakalova, G. Argentero, T. Pennycook, J. C. Meyer, A. Fejfar, A. Kromka, B. Rezek, *J. Phys. Chem. C* **2015**, *119*, 27708.
[60] Z. Weiss, *J. Anal. At. Spectrom.* **2015**, *30*, 1038.
[61] H. Takahara, R. Ishigami, K. Kodama, A. Kojyo, T. Nakamura, Y. Oka, *J. Anal. At. Spectrom.* **2016**, *31*, 940.
[62] M. M. Brzhezinskaya, A. S. Vinogradov, A. V. Krestinin, G. I. Zvereva, A. P. Kharitonov, I. I. Kulakova, *Phys. Solid State* **2010**, *52*, 876.
[63] M. Brzhezinskaya, V. Shmatko, G. Yalovega, A. Krestinin, I. Bashkin, E. Bogoslavskaja, *J. Electron Spectrosc. Relat. Phenom.* **2014**, *196*, 99.
[64] H. Girard, N. Simon, D. Ballutaud, M. Herlem, A. Etcheberry, *Diamond Relat. Mater.* **2007**, *16*, 316.
[65] S.-G. Ri, D. Takeuchi, H. Kato, M. Ogura, T. Makino, S. Yamasaki, H. Okushi, B. Rezek, C. E. Nebel, *Appl. Phys. Lett.* **2005**, *87*, 262107.
[66] A. A. Eliseev, N. I. Verbitskiy, A. A. Volykhov, A. V. Fedorov, O. Y. Vilkov, I. I. Verbitskiy, M. M. Brzhezinskaya, N. A. Kiselev, L. V. Yashina, *Carbon* **2016**, *99*, 619.
[67] G. Zhang, T. Samuely, H. Du, Z. Xu, L. Liu, O. Onufriienko, P. W. May, J. Vanacken, P. Szabó, J. Kačmarčík, H. Yuan, P. Samuely, R. E. Dunin-Borkowski, J. Hofkens, V. V. Moshchalkov, *ACS Nano* **2017**, *11*, 11746.
[68] G. Zhang, S. D. Janssens, J. Vanacken, M. Timmermans, J. Vacík, G. W. Ataklti, W. Decelle, W. Gillijns, B. Goderis, K. Haenen, P. Wagner, V. V. Moshchalkov, *Phys. Rev. B* **2011**, *84*, 214517.
[69] D. Koh, S. K. Banerjee, J. Brockman, M. Kuhn, S. W. King, *Diamond Relat. Mater.* **2020**, *101*, 107647.
[70] F. Maier, R. Graupner, M. Hollering, L. Hammer, J. Ristein, L. Ley, *Surf. Sci.* **1999**, *443*, 177.
[71] B. P. Reed, M. E. Bathen, J. W. R. Ash, C. J. Meara, A. A. Zakharov, J. P. Goss, J. W. Wells, D. A. Evans, S. P. Cooil, *Phys. Rev. B* **2022**, *105*, 205304.
[72] P. John, N. Polwart, C. E. Troupe, J. I. B. Wilson, *Diamond Relat. Mater.* **2002**, *11*, 861.
[73] J. I. B. Wilson, J. S. Walton, G. Beamson, *J. Electron Spectrosc. Relat. Phenom.* **2001**, *121*, 183.
[74] S. Chaudhuri, S. J. Hall, B. P. Klein, M. Walker, A. J. Logsdail, J. V. Macpherson, R. J. Maurer, *Commun. Mater.* **2022**, *3*, 6.
[75] P. K. Baumann, R. J. Nemanich, *Surf. Sci.* **1998**, *409*, 320.
[76] J. Ryl, M. Cieslik, A. Zielinski, M. Ficek, B. Dec, K. Darowicki, R. Bogdanowicz, *Materials* **2020**, *13*, 964.
[77] A. Denisenko, C. Pietzka, A. Romanyuk, H. El-Hajj, E. Kohn, *J. Appl. Phys.* **2008**, *103*, 014904.
[78] M. Pumera, *Nanomaterials for Electrochemical Sensing and Biosensing*, CRC Press, Boca Raton, FL **2014**.
[79] R. G. Compton, E. Kätelhön, K. R. Ward, E. Laborda, *Understanding Voltammetry: Simulation of Electrode Processes*, World Scientific (Europe), Singapore **2020**.
[80] T. J. Davies, R. G. Compton, *J. Electroanal. Chem.* **2005**, *585*, 63.
[81] M. Da Rocha, B. Dunn, A. Rougier, *Sol. Energy Mater. Sol. Cells* **2019**, *201*, 110114.
[82] V. Augustyn, P. Simon, B. Dunn, *Energy Environ. Sci.* **2014**, *7*, 1597.
[83] J. Wang, J. Polleux, J. Lim, B. Dunn, *J. Phys. Chem. C* **2007**, *111*, 14925.
[84] R. Giannuzzi, R. Scarfiello, T. Sibillano, C. Nobile, V. Grillo, C. Giannini, P. D. Cozzoli, M. Manca, *Nano Energy* **2017**, *41*, 634.
[85] A. Olejnik, M. Ficek, M. Szkodo, A. Stanisławska, J. Karczewski, J. Ryl, A. Dołęga, K. Siuzdak, R. Bogdanowicz, *ACS Nano* **2022**, *16*, 13183.
[86] A. J. Bard, *J. Am. Chem. Soc.* **2010**, *132*, 7559.
[87] T. Ando, K. Asai, J. Macpherson, Y. Einaga, T. Fukuma, Y. Takahashi, *Anal. Chem.* **2021**, *93*, 5831.
[88] M. Sobaszek, K. Siuzdak, J. Ryl, M. Sawczak, S. Gupta, S. B. Carrizosa, M. Ficek, B. Dec, K. Darowicki, R. Bogdanowicz, *J. Phys. Chem. C* **2017**, *121*, 20821.
[89] J. Ryl, L. Burczyk, R. Bogdanowicz, M. Sobaszek, K. Darowicki, *Carbon* **2016**, *96*, 1093.
[90] A. Nefedov, C. Wöll, in *Surface Science Techniques*, (Eds.: G. Bracco, B. Holst), Springer, Berlin, Heidelberg **2013**, pp. 277–303.
[91] M. Brzhezinskaya, A. Irzhak, D. Irzhak, T. W. Kang, O. Kononenko, V. Matveev, G. Panin, D. Roshchupkin, *Phys Status Solidi Rapid Res Lett* **2016**, *10*, 639.

[92] M. Brzhezinskaya, O. Kononenko, V. Matveev, A. Zotov, I. I. Khodos, V. Levashov, V. Volkov, S. I. Bozhko, S. V. Chekmazov, D. Roshchupkin, *ACS Nano* **2021**, *15*, 12358.
[93] M. Brzhezinskaya, I. V. Mishakov, Y. I. Bauman, Y. V. Shubin, T. A. Maksimova, V. O. Stoyanovskii, E. Y. Gerasimov, A. A. Vedyagin, *Appl. Surf. Sci.* **2022**, *590*, 153055.
[94] A. L. Pomerantsev, *Progress in Chemometrics Research*, Nova Publishers, Hauppage, NY **2005**.
[95] M. J. van Setten, M. Giantomassi, E. Bousquet, M. J. Verstraete, D. R. Hamann, X. Gonze, G.-M. Rignanese, *Comput. Phys. Commun.* **2018**, *226*, 39.
[96] S. Smidstrup, T. Markussen, P. Vancraeyveld, J. Wellendorff, J. Schneider, T. Gunst, B. Verstichel, D. Stradi, P. A. Khomyakov, U. G. Vej-Hansen, M.-E. Lee, S. T. Chill, F. Rasmussen, G. Penazzi, F. Corsetti, A. Ojanperä, K. Jensen, M. L. N. Palsgaard, U. Martinez, A. Blom, M. Brandbyge, K. Stokbro, *J. Phys.: Condens. Matter* **2019**, *32*, 015901.
[97] J. E. Sipe, E. Ghahramani, *Phys. Rev. B* **1993**, *48*, 11705.
[98] D. Porezag, M. R. Pederson, *Phys. Rev. B* **1996**, *54*, 7830.
[99] T. Ozaki, *Phys. Rev. B* **2003**, *67*, 155108.
[100] M. Cococcioni, S. de Gironcoli, *Phys. Rev. B* **2005**, *71*, 035105.